Research

A SCIENCE PARTNER JOURNAL

Review Article

High-Performance $Mg_3Sb_{2-x}Bi_x$ Thermoelectrics: Progress and Perspective

Airan Li,[1] **Chenguang Fu** [iD]**,**[2] **Xinbing Zhao** [iD]**,**[1] **and Tiejun Zhu** [iD][1]

[1]*State Key Laboratory of Silicon Materials, School of Materials Science and Engineering, Zhejiang University, 310027 Hangzhou, China*
[2]*Max Planck Institute for Chemical Physics of Solids, Nöthnitzer Str. 40, 01187 Dresden, Germany*

Correspondence should be addressed to Chenguang Fu; chenguang.fu@cpfs.mpg.de and Tiejun Zhu; zhutj@zju.edu.cn

Since the first successful implementation of *n*-type doping, low-cost $Mg_3Sb_{2-x}Bi_x$ alloys have been rapidly developed as excellent thermoelectric materials in recent years. An average figure of merit zT above unity over the temperature range 300–700 K makes this new system become a promising alternative to the commercially used *n*-type $Bi_2Te_{3-x}Se_x$ alloys for either refrigeration or low-grade heat power generation near room temperature. In this review, with the structure-property-application relationship as the mainline, we first discuss how the crystallographic, electronic, and phononic structures lay the foundation of the high thermoelectric performance. Then, optimization strategies, including the physical aspects of band engineering with Sb/Bi alloying and carrier scattering mechanism with grain boundary modification and the chemical aspects of Mg defects and aliovalent doping, are extensively reviewed. Mainstream directions targeting the improvement of zT near room temperature are outlined. Finally, device applications and related engineering issues are discussed. We hope this review could help to promote the understanding and future developments of low-cost $Mg_3Sb_{2-x}Bi_x$ alloys for practical thermoelectric applications.

1. Introduction

Thermoelectric (TE) materials, which can convert heat into electric energy or vice versa without any moving parts, provide a promising solution to the current energy crisis [1]. In order to enable more practical applications in power generation and solid-state cooling, the key challenge is to improve the performance of TE materials, which is usually gauged by the dimensionless figure of merit, zT, $zT = S^2\sigma T/(\kappa_L + \kappa_e)$, where S, σ, T, κ_L, and κ_e are the Seebeck coefficient, electrical conductivity, absolute temperature, and lattice and electronic components of thermal conductivity κ, respectively [2]. Aiming at obtaining a high zT, there are two primary directions in the TE research: one is to optimize the TE properties of established good materials mainly through the band and phonon engineering strategies [3, 4]; the other is to discover novel promising candidates based on the instruction of theoretical predictions or trial and error [5, 6].

With a constant endeavor of thermoelectricians in the past decades, more than ten semiconductor systems have been exploited with high zT above unity, some even higher

than 2, e.g., V_2VI_3 compounds [7–10], IV-VI compounds [11–18], transition metal chalcogenides [19, 20], half-Heusler compounds [21–26], skutterudites [27–29], Zintl compounds [30–33], clathrates [34, 35], metal silicides [36–38], and $Si_{1-x}Ge_x$ alloys [39, 40]. Among these good TE systems, most of them exhibit peak zT in the moderate-to-high temperature range (≥600 K), of which the practical applications would be power generation. In contrast, TE materials with high zT near room temperature (RT) are superior candidates for both low-grade heat power generation and solid-state cooling. Regarding cooling applications, there is a big market demand in a variety of industries, such as healthcare, automotive, semiconductors, and electronics. The global solid-state cooling market is estimated to be valued at USD 395 million in 2019 and is predicted to reach USD 641 million by 2024 [41]. Hence, the development of low-cost TE materials with high zT near RT is highly desirable.

Since the discovery in the mid-twentieth century [42], V_2VI_3 compounds [9, 43], including Bi_2Te_3, Sb_2Te_3, and Bi_2Se_3, and their solid solutions, have long been the best TE

TABLE 1: Basic physical and chemical information for the elements in the two n-type near-RT $Mg_3Sb_{2-x}Bi_x$ and $Bi_2Te_{3-x}Se_x$ thermoelectrics. Oxygen is also included since it is often found in the synthesized samples. Most data are obtained from WebElements [101] while Shannon-Prewitt radii from KnowledgeDoor [102].

Element	Mg	Sb	Bi	Te	Se	O
Atomic number	12	51	83	52	34	8
Density (g/cm^3)	1.738	6.697	9.78	6.24	4.819	—
Abundances (ppm by weight)	29000	0.2	0.025	0.001	0.05	460000
Melting point (˚C)	650	630.63	271.3	449.51	221	-218.3
Boiling point (˚C)	1090	1387	1564	988	685	-182.9
Electronic configuration	$3s^2$	$5s^2\,5p^3$	$6s^2\,6p^3$	$5s^2\,5p^4$	$4s^2\,4p^4$	$2s^2\,2p^4$
Electronegativity (Pauling)	1.31	2.05	2.02	2.1	2.55	3.44
Atomic radius (Å)	1.5	1.45	1.6	1.4	1.15	0.6
Pauling ionic radius (Å)	0.65 Mg^{2+}	—	—	2.21 Te^{2-}	1.98 Se^{2-}	1.4 O^{2-}
Shannon-Prewitt radius (Å) (coordination number)	0.72 Mg^{2+}(6)	0.76 Sb^{3+}(6)	1.03 Bi^{3+}(6)	2.21 Te^{2-}(6)	1.98 Se^{2-}(6)	1.40 O^{2-}(6)

materials near RT, being the primary choice for the commercial cooling application. However, the relatively scarce element tellurium (see Table 1) is a potential impediment for the large-scale TE applications of V_2VI_3 compounds. In recent years, Mg-based semiconductors, e.g., p-type α-MgAgSb [44–46] and n-type $Mg_3Sb_{2-x}Bi_x$ [33, 47, 48], have been discovered with good TE performance near RT, comparable to V_2VI_3 compounds. Magnesium is the 8th most abundant element in the earth's crust [49]. TE materials containing low-cost magnesium could thus have a better prospect for large-scale applications.

Historically, the exploration of Mg-based TE materials began with Mg_2Si-based compounds in the 1960s [50]. By alloying with Sn or Ge, the resulted band convergence and point defect scattering contribute to a peak zT above unity in $Mg_2Si_{1-x}Sn_x$ and $Mg_2Ge_{1-x}Sn_x$ solid solutions [36, 37, 51, 52]. A series of work has also been conducted to optimize their TE performance, including introducing dislocations and point defects [53–55]. In 2012, the TE properties of another Mg-based compound α-MgAgSb, which belongs to the Nowotny-Juza family [56], were reported by Kirkham et al. [44]. The synthesized α-MgAgSb sample with unignorable impurity phases still exhibits a potential zT of 0.56 at around 400 K. Later, by improving phase purity, a peak zT above unity was obtained in p-type MgAgSb samples by several groups [45, 46, 57, 58]. The hierarchical chemical bonding in α-MgAgSb leads to strong anharmonicity and intrinsically low sound velocity [59], which are responsible for the low thermal conductivity κ and high zT near RT [45, 46, 57]. However, MgAgSb has a complex phase transition process when cooling from its liquid state with two phase transition points at around 360˚C and 300˚C, respectively [60]. Additionally, the binary impurity phase, for instance, Ag_3Sb, is also easily formed during the synthesis. These make it difficult to synthesize the high-purity α-MgAgSb (room temperature phase); particularly, the single crystal is not yet reported. Moreover, the high TE performance in α-MgAgSb is only obtained when doping it as p-type, and there is still no experimental report on successful electron doping.

Intermetallic compound Mg_3X_2 (X = Sb, Bi) was first reported by Zintl and Husemann in the 1930s [61], later being classified as a member of Zintl phase compounds [62]. The elec-

trical transport behavior of Mg_3X_2 was studied by Pincherle and Radcliffe in the 1950s [63]. Mg_3Sb_2 exhibited a p-type semiconducting behavior with an energy gap (E_g) of 0.8 eV while Mg_3Bi_2 showed metallic behavior. The study on the TE properties of Mg_3X_2 began in the 2000s [64]. Despite the low κ and inexpensive raw elements, its p-type semiconducting behavior and inferior TE performance do not make it a good TE material [65–69]. In 2016, $Mg_3Sb_{2-x}Bi_x$ compounds were discovered to be a new promising n-type TE system by exhibiting a peak zT of 1.5 at around 700 K [70–73], more than twice higher than that of the p-type counterparts (Figure 1(a)). This exciting result also makes n-type $Mg_3Sb_{2-x}Bi_x$ standing out of the Zintl phase TE family, of which the family members are generally exhibiting good p-type TE properties, even rarely been electron-doped [74]. The successful realization of n-type $Mg_3Sb_{2-x}Bi_x$ results from the understanding of the Mg defect chemistry, and the Bi alloying promoted electron doping by reducing the bandgap [70, 71]. That is, only in the Mg-rich environment, for instance, adding slightly excess Mg in the raw experimental design, can n-type $Mg_3Sb_{2-x}Bi_x$ be obtained. Actually, this excess Mg supportive electron doping has been recognized in synthesizing n-type $Mg_2Si_{1-x}Sn_x$ TE materials previously, where excess Mg was thought to compensate the loss of Mg during the synthesis, and additionally, some excess Mg atoms could enter into the interstitial sites facilitating electron doping [54, 75, 76]. The role of excess Mg in $Mg_3Sb_{2-x}Bi_x$ is mainly suppressing the Mg vacancies while Mg interstitial is difficult to form, which will be discussed in detail in the later section.

Despite exhibiting a high zT of 1.5 at around 700 K, the power generators made from n-type $Mg_3Sb_{2-x}Bi_x$ might be challenging owing to the decomposition of the compounds and possible deterioration of electrical properties at elevated temperatures [90, 91]. Fortunately, even near RT, n-type $Mg_3Sb_{2-x}Bi_x$ also shows good zT of around 0.8 (Figure 1(b)), making it a promising alternative to the state-of-the-art n-type $Bi_2Te_{3-x}Se_x$ for solid-state cooling application. Although only 4 years have passed since the discovery of n-type $Mg_3Sb_{2-x}Bi_x$, there are already many important advances achieved, including the improvement of TE performance [33, 48, 70–73, 78–80, 82, 92, 93], the understanding of the origin for good power factor [70, 71] and intrinsically low κ [94], the revelation of the
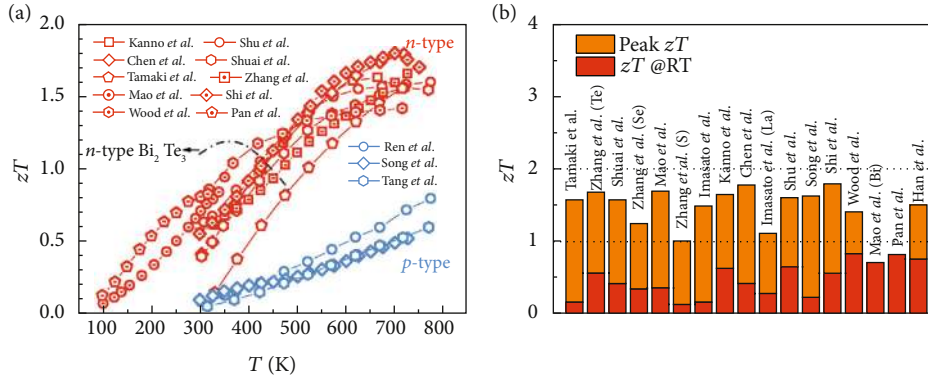
FIGURE 1: (a) Temperature-dependent zT for both n-type and p-type $Mg_3Sb_{2-x}Bi_x$-based TE materials. The data are taken from Refs. [33, 48, 70–73, 77–83]. As a comparison, the zT of n-type $Bi_2Te_{3-x}Se_x$ is also shown [8]. (b) The peak and room temperature zT for n-type $Mg_3Sb_{2-x}Bi_x$. The data are taken from Refs. [33, 48, 70–73, 80, 82, 84–89].

carrier scattering mechanism near RT [82, 95, 96], the increasing awareness of Mg defect chemistry [70, 97, 98], and even the successful attempt of TE module [33].

The advances in n-type $Mg_3Sb_{2-x}Bi_x$ demonstrate a good paradigm of how a new TE material can be rapidly developed and even transferred into the lab-scale module verification by the current TE community. In the past two years, there have been two timely review articles discussing the recent progress of Mg_3Sb_2 and its derivatives: one is focusing on the design principle with a combination of theory and experiment [99] and the other on the manipulation of defects and electronic transport properties [100]. Readers who are interested in more details may refer to these two reviews. In this review, we focus on recent progress and perspective of the TE performance enhancement near RT. Started with the understanding of basic information of $Mg_3Sb_{2-x}Bi_x$, the bonding and crystal structure, electronic structure, and phonon dispersion are discussed to reveal the intrinsic foundation of the transport properties. Then, several important aspects, including band engineering with Sb/Bi alloying, carrier scattering mechanism near room temperature, Mg defect chemistry, and extrinsic doping which affect the TE performance near RT, are summarized. Finally, we discuss the thermal stability of this system, which is a key step towards practical applications. We hope this review could help to promote the development of $Mg_3Sb_{2-x}Bi_x$ for future TE applications near RT.

2. Chemical Bonding and Structure

2.1. Basic Information about the Constituent Elements. The structure-property relationship is essential to understand and design advanced materials for practical applications. Here, before the comprehensive discussions of the structure-property relationship in the $Mg_3Sb_{2-x}Bi_x$ system, we first make a list of the basic physical and chemical properties of the elements Mg, Sb, Bi, Te, and Se (Table 1), making up the two near-RT TE systems, $Mg_3Sb_{2-x}Bi_x$ and $Bi_2Te_{3-x}Se_x$. Several important points, which will be frequently referred to in the following sections, are first highlighted here. (i) The density of Mg is much smaller than that of Sb, Bi, Te, and Se. This could be an advantage of lightweight for n-type $Mg_3Sb_{2-x}Bi_x$ used for TE modules, compared to commercial $Bi_2Te_{3-x}Se_x$. (ii) The melting point of Mg is the

highest one among the listed elements. However, its lower boiling point, compared to Sb and Bi, suggests a higher vapor pressure and a potentially larger loss of Mg for $Mg_3Sb_{2-x}Bi_x$ at elevated temperatures [103]. (iii) The Pauling electronegativity (EN) of Mg is only 1.31, much smaller compared to O (3.44), suggesting the high reactivity of Mg metal. In the atmosphere, the surface of Mg metal is soon coated with a thin layer of oxide that partly inhibits reactivity, the so-called passivation. The passivation and high vapor pressure of Mg could be reasons why the actual compositions of the synthesized $Mg_3Sb_{2-x}Bi_x$ compounds are generally Mg-deficient if being nominally designed. (iv) The electronic configuration of Mg is $3s^2$, and hence, Mg usually has a +2 oxidation state in the ambient environment. The Pauling ionic radius of Mg^{2+} is 0.65 Å, which is much smaller than that of the Sb and Bi anions (their Pauling ionic radii are not available but should be larger than their atomic radii, by referring to the difference in the atomic and ionic radii of Te, Se, and O). This diminutive radius of Mg^{2+}, even comparable to that of Li^+ (0.6 Å), was thought to be one of the structural reasons leading to weak interlayer bonding and thus intrinsically low κ in Mg_3Sb_2 and Mg_3Bi_2 [94]. Additionally, this is perhaps also why Mg_3Bi_2 has also attracted attention as candidates for superionic conductor [104, 105] and Mg-ion battery [106, 107]. Furthermore, although having not been thoroughly studied, this diminutive radius of Mg^{2+} might also relate to the thermal instability of this system when working at elevated temperatures. (v) The difference in Pauling EN for the constituent elements of Mg_3Sb_2 is 0.74 (0.71 for Mg_3Bi_2), which is much larger that of Bi_2Te_3 (0.08) and the other good thermoelectrics, such as Sb_2Te_3 (0.05), PbTe (0.23), PbSe (0.22), GeTe (0.09), SnTe (0.14), SnSe (0.59), SiGe (0.11), Mg_2Si (0.59), and ZnSb (0.4). This is an indication that the chemical bond of Mg_3Sb_2 and Mg_3Bi_2 has a larger component of ionic character, compared to above mentioned good thermoelectrics.

2.2. Crystal Structure. Mg_3Sb_2 and Mg_3Bi_2 crystallize in a trigonal anti-α-La_2O_3 type structure (space group $P\bar{3}m1$) below 1203 K and 976 K, respectively [108]. A cubic Mn_2O_3-type structure (space group $Ia\bar{3}$) was reported in some literature for Mg_3X_2 above the transition temperatures
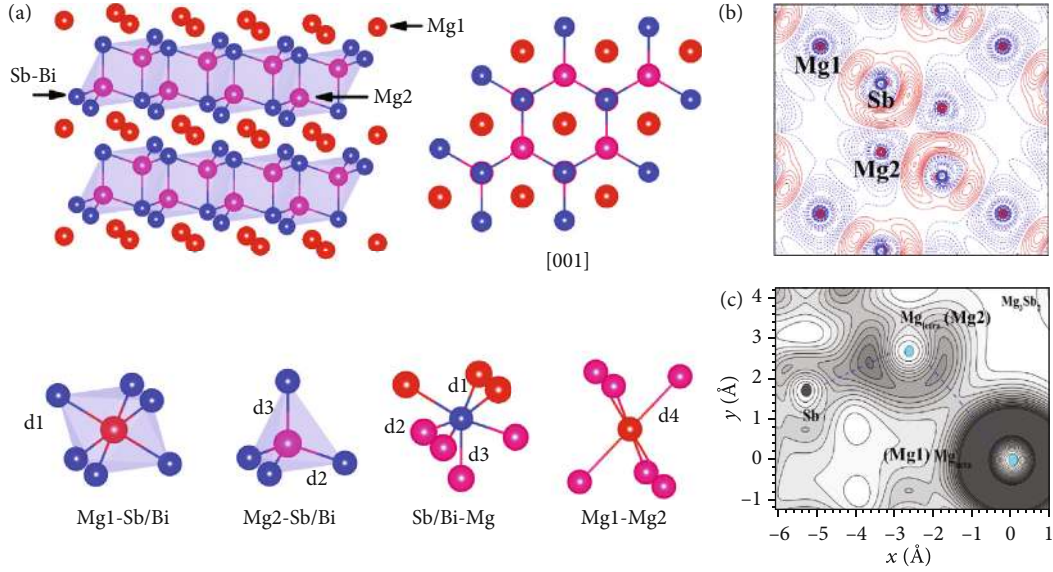
FIGURE 2: (a) Crystal structure of Mg_3X_2, the right figure is viewed from [001] direction. Drawn using *VESTA* [125]. The coordination of Mg1, Mg2, and X is presented below the crystal structure. (b) Static deformation electron density map on (110) plane of Mg_3Sb_2. (c) The partial charge densities for Mg_3Sb_2. Panel (b) is reproduced with permission from Ref. [121]. CC-BY-4.0. Panel (c) is reproduced with permission from Ref. [116]. Copyright 2019 Wiley Periodicals, Inc.

TABLE 2: Lattice parameter and bond length between adjacent atoms for Mg_3X_2. The data are taken from Refs. [61, 108, 110–112].

Mg_3Sb_2			Mg_3Bi_2		
Lattice parameter (Å)		Reference	Lattice parameter (Å)		Reference
a	c		a	c	
4.573	7.229	[61]	4.671	7.403	[61]
4.568 ± 0.003	7.229 ± 0.004	[108]	4.666	7.401	[110]
4.547(5)	7.235(3)	[111]	4.645(3)	7.380(3)	[111]
Bond length (Å)					
Mg1-Sb(d1)	3.111		Mg1-Bi(d1)	3.1403	
Mg2-Sb(d2)	2.819	[108]	Mg2-Bi(d2)	2.9132	[112]
Mg2-Sb(d3)	2.933		Mg2-Bi(d3)	2.9900	
Mg1-Mg2(d4)	3.736		Mg1-Mg2(d4)	—	

[109]. For Mg_3Bi_2, a neutron powder diffraction was carried out to determine the high-temperature phase by Barnes et al. [104]. A phase transition from the α phase (low temperature) to the β phase was observed at $T = 730 \pm 10°C$. The β-Mg_3Bi_2 was determined to be a body-centered cubic structure. However, to our best survey of the literature, there is still no convincing structural information of β-Mg_3Sb_2. We tried to quench Mg_3Sb_2 and Mg_3Bi_2 samples into liquid nitrogen from temperature above 1203 K and 976 K, respectively. However, with the XRD measurement, the quenched crystals still show a trigonal structure without a trace of cubic structure, suggesting the phase transition might be fairly quick.

The crystal structure of trigonal Mg_3X_2 and the corresponding lattice parameters and bond lengths are shown in Figure 2(a) and Table 2, respectively. Under the Zintl concept, Mg_3X_2 can also be classified into the $CaAl_2Si_2$-type structure by rewriting it as $MgMg_2X_2$ [94]. Mg atoms take two different sites in the lattice: one is at the octahedral site surrounded by

six X atoms, named as the Mg1 atom, and the other is at the tetrahedral site surrounded by four X atoms, named as the Mg2 atom. The Mg1 atom shows the most electropositive character and provides 2 electrons to the covalent bounded $Mg_2X_2^{2-}$ network. This configuration not only provides a rough diagram to understand the structure-property relationship of Mg_3X_2 but also gives instruction about the site preference when alloying with other elements [113]. The Mg1 sites are favorably occupied when alloying with more electropositive alkaline earth metals and lanthanides, like Ca, Sr, Ba, La, and Yb [114–118], whereas Mg2 sites with more electronegative Zn, Mn, and Cd metals [119, 120].

Recently, Zhang et al. [99] performed a quantitative chemical bonding analysis of Mg_3Sb_2, from which they found that Mg1 and Mg2 atoms show close bonding character with the Sb atom with the atomic charge of +1.51 and +1.47, respectively (Figure 2(b)). The interlayer interaction in Mg_3Sb_2 is largely ionic with partial covalent nature, which
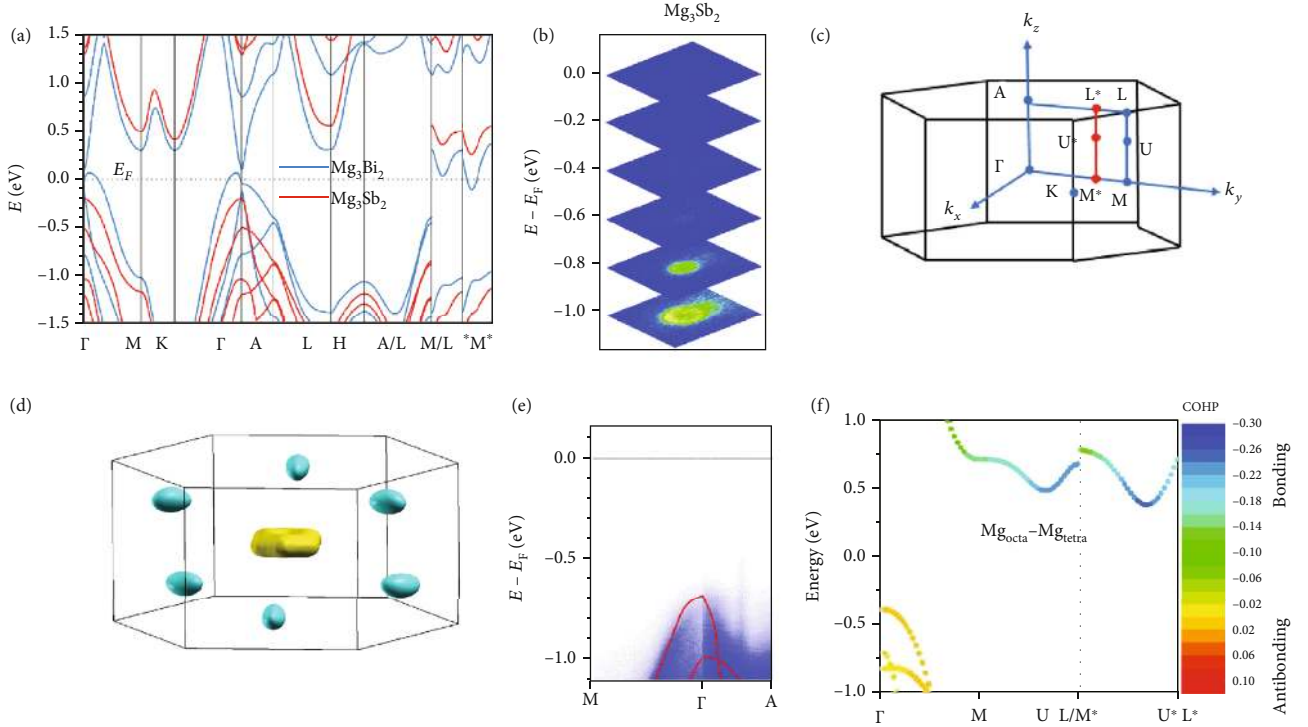
FIGURE 3: (a) Band structure of Mg_3Sb_2 and Mg_3Bi_2. (b) A series of constant energy maps of Mg_3Sb_2 by ARPES. (c) Brillouin zone (BZ) and high-symmetry points in BZ of the trigonal structure of Mg_3X_2. (d) The diagram of Fermi surfaces of Mg_3Bi_2. (e) ARPES spectra along the high-symmetry directions of Mg_3Sb_2, the red line is the corresponding calculated band structures. (f) The band-resolved projected Crystal Orbital Hamiltonian Population (COHP) for the interaction between Mg1 and Mg2 in Mg_3Sb_2. Panels (a, b, d, e) are reproduced with permission from Ref. [48]. Published by The Royal Society of Chemistry. Panel (f) is reproduced with permission from Ref. [116]. Copyright 2019 Wiley Periodicals, Inc.

is comparable to the intralayer interaction with the same type of bond [121]. These calculations give a rational explanation of the nearly isotropic thermal properties of Mg_3X_2 along the ab-plane and c-axis. These nearly isotropic thermal properties make Mg_3X_2 different from the other $CaAl_2Si_2$-type Zintl compounds, such as $CaZn_2Sb_2$ and $SrZn_2Sb_2$, showing anisotropic thermal properties [121]. With these findings, Zhang et al. argued the breakdown of the Zintl formalism in the AMg_2X_2 system (A is an alkaline earth or a divalent rare earth element) [99], arousing the debate as to whether Mg_3Sb_2 is a Zintl phase [121, 122]. To address the debate, it is necessary to recall the definition of a Zintl phase. AB_2X_2 compounds with $CaAl_2Si_2$-type structure were defined, by Hoffmann et al. [113, 123], as Zintl phases since the structure can be described as the covalently bonded $[B_2X_2]^{\delta-}$ networks receiving electrons donated by the ionic $A^{\delta+}$ cations. In these compounds, the clear coexistence of the ionic cation and covalent anionic network is therefore the key feature of the Zintl phase and widely applied Zintl concept. Moreover, Kauzlarich et al. have also given a comprehensive discussion and historical review on the definition of Zintl phases [124], which can be referred to as the intermetallic compounds with mixed chemical bonding character of ionic and covalent bonds, generally composed of electropositive metal (alkali metal, alkaline earth element, and lanthanide) and posttransition metal or metalloid (i.e., from groups 13, 14, 15, or 16). From this point of review, it is not appropriate to consider Mg_3Sb_2 as Zintl phases as both the cationic and anionic parts are nearly ionic

[99] although they are charge-balanced and the electron-counting rule is still applicable. It should be noted that the definition of the Zintl phase and Zintl concept discussed here is, in the narrow sense, the definition made by Hoffmann et al. [113, 123] and Kauzlarich et al. [124].

In addition to the Mg-Sb interactions, the calculations by Sun et al. [116] show that there exists a bonding interaction between the Mg1 and Mg2 atoms, in the conduction band minimum (CBM) region (Figure 2(c)). Since the distance between Mg1 and Mg2 is fairly large (Table 2) and also their close atomic charge [121], this interaction between 3s levels of Mg1 and Mg2 would be much weaker than that of Mg-Sb bonds. In short, compared to the typical $CaAl_2Si_2$-type Zintl compounds, the chemical bonding of Mg_3X_2 shows a nearly isotropic character in the Mg-Sb bonds between the interlayer and intralayer and an additional Mg1-Mg2 interaction at the CBM. This unique bonding character in Mg_3X_2, partly originating from the similar chemical environment of Mg1 and Mg2 atoms, is crucial to understand their electronic and phononic structures and thus the electrical and thermal transport properties.

2.3. Electronic Structure.

We now move to understand the electronic structure of Mg_3X_2. The calculated band structures of Mg_3Sb_2 and Mg_3Bi_2 are juxtaposed in Figure 3(a). Mg_3Sb_2 is an indirect semiconductor with the calculated bandgap E_g ranging from 0.4 to 0.7 eV based on different calculation methods [70, 71, 110, 116, 126, 127], while

Mg_3Bi_2 is predicted to be a topological nodal line semimetal with the coexistence of electron and hole pockets near Fermi level E_F [128–130]. Experimentally, an E_g of about 0.18 eV was estimated from the resistivity below 390 K for undoped Mg_3Sb_2 [131], while a much larger value of about 0.8 eV was reported by estimating the gap of the liquid phase of Mg_3Sb_2 [132]. A similar E_g of 0.8 eV was also reported in the 1950s [63]. The Fourier transform infrared spectroscopy measurement was performed to estimate the optical gap of $Mg_3Sb_{2-x}Bi_x$ solid solutions, yielding a similar value of about 0.28 eV for $Mg_3Sb_{1.5}Bi_{0.5}$ [80] and Mg_3SbBi [92]. Additionally, a direct revelation of the E_g for a semiconductor is possible by carrying out the angle-resolved photoemission spectroscopy (ARPES) on its n-type single crystals [26]. Pan et al. recently reported the ARPES study on n-type Mg_3Sb_2 single crystal, from which a forbidden gap is clearly observed (Figure 3(b)) and an E_g > 0.6 eV is estimated for Mg_3Sb_2 [48]. But since the conduction band was not observed, further study is necessary to accurately determine the real E_g. The ARPES study was also performed for Mg_3Bi_2 single crystal, and its semimetal feature was confirmed [129].

From Figure 3(a), it is easily observed that the valence band maximum (VBM) of both Mg_3Sb_2 and Mg_3Bi_2 is near the Γ point, the center of the first Brillouin zone (Figure 3(c)). In contrast, the conduction band minimum (CBM) of Mg_3X_2 locates at the U* point in the M*L* direction, away from the high-symmetry points. To simultaneously demonstrate the shape and valley number of VBM and CBM, the Fermi surfaces of Mg_3Bi_2 are provided (Figure 3(d)). There are two distinct features in the VBM and CBM of Mg_3Bi_2. First, there are six electron pockets but only one hole pocket, suggesting a high band degeneracy N_v of 6 in CBM and a low N_v of 1 in VBM. High N_v is usually thought to be beneficial for high TE performance since the zT is proportional to the expression $\mu N_v m_b^{*3/2}/\kappa_L$ [11, 21], where μ is the carrier mobility and m_b^* is the single-band effective mass. The difference in band degeneracy of CBM and VBM might explain why $Mg_3(Sb,Bi)_2$ shows better n-type TE performance [70, 71], as shown in Figure 1(a).

Another distinct feature is that the six electron pockets are nearly spherical while the hole pocket shows an obvious anisotropy along the k_x-k_y plane and k_z direction. This anisotropy in VBM is well embodied in the calculated effective masses along the two directions [71, 133, 134]. For example, in the calculation by Zhang et al., m_{xx}^* (m_{yy}^*) was estimated to be $1.15m_e$ and m_{zz}^* is $0.15m_e$ [71]. It is worth mentioning that the band anisotropy has recently been experimentally confirmed via the ARPES study on the Mg_3Sb_2 single crystal (Figure 3(e)), giving different effective masses of $0.9m_e$ and $0.16m_e$ along the two directions, respectively [48]. Moreover, a single crystal study on Mg_3Bi_2 had also confirmed this valence band anisotropy by measuring the electrical resistivity ρ along the ab-plane and c-axis, where the ab-plane was found to show a twice larger ρ [135]. The ρ along the ab-plane and c-axis was also reported for the Mg_3Sb_2 single crystals. However, since the studied single crystals were undoped ones and the very high ρ indicates that the Fermi level still lies in the for-

bidden gap, the band anisotropy on the VBM of Mg_3Sb_2 cannot be concluded [135]. The hole-doped Mg_3Sb_2 single crystals are required to observe the anisotropy in electrical transport along the ab-plane and c-axis.

Regarding the high N_v in the CBM of Mg_3X_2, another interesting question arises as to why the CBM locates off the high-symmetry points. This is an important question awaiting answers. If CBM locates at the U point, the electron pockets will be shared by the second Brillouin zone, and thus, the band degeneracy in the CBM will halve. One possible answer is traced to the electron structure calculation by Sun et al. [116], where they reported on a bonding interaction between the Mg1 and Mg2 atoms in the CBM region of Mg_3Sb_2, which is particularly stronger in the U* point than the other positions (Figure 3(f)). Even further, Han et al. recently found that this Mg1-Mg2 interaction in Mg_3Sb_2 can be even weakened by replacing Sb with Bi to increase the Mg1-Mg2 distance, leading to a more dispersive CBM although its position is still at the U* point [89]. Therefore, the unique Mg1-Mg2 interaction in Mg_3X_2 might be related to the origin of the CBM position, but further studies, both theoretically and experimentally, are still necessary before drawing a convincing conclusion. An experimental study of the CBM of Mg_3X_2 and the solid solution $Mg_3Sb_{0.75}Bi_{1.25}$ by ARPES was attempted by Pan et al. [48]. Although their single crystals are all electron-doped with the carrier concentration n in the magnitude of 10^{19} cm^{-3}, there is still no obvious electron pocket observed in the first Brillouin zone by ARPES. This indicates that higher electron-doped single crystals with n over 10^{20} cm^{-3} are necessary to experimentally reveal the CBM by ARPES.

2.4. Phononic Band Structure.

Besides the high N_v, the other key reason leading to the high TE performance of n-type $Mg_3Sb_{2-x}Bi_x$ is their low κ_L. Figure 4(a) presents the experimental κ_L for both single-crystalline and polycrystalline Mg_3X_2 and their solid solutions. In most experimental reports, the κ_L of Mg_3X_2 at room temperature is smaller than 2 W m^{-1} K^{-1}, which is comparable to that of Bi_2Te_3. This "anomalously" low κ_L of Mg_3X_2 is to some extent unexpected, considering its simple crystal structure and the light element Mg. In general, compounds with a complex crystal structure, i.e., a large number of atoms in the unit cell, often have intrinsically low κ_L, because the considerable optical phonons in complex structures suppress the frequency of the acoustic phonons in the phase space and result in low group velocity of acoustic modes [136]. Compounds with heavy elements can also have low κ_L due to the low sound velocity of the acoustic phonons [137]. However, Mg_3X_2 has a simple crystal structure with only five atoms in the unit cell, and thus, the origin of its low κ_L becomes a very important question. The phononic band structure of pure Mg_3Sb_2 was reported by Peng et al. [94]. As shown in Figure 4(b), the thickness of the lines with colors represents the degree of anharmonicity. For the low-frequency acoustic branch, Mg_3Sb_2 shows a large degree of anharmonicity. If only taking the phonon-phonon Umklapp scattering into account, κ_L is proportional to the expression $A\bar{M}\theta_D\delta^3/(\gamma^2 N^{2/3}T)$, where
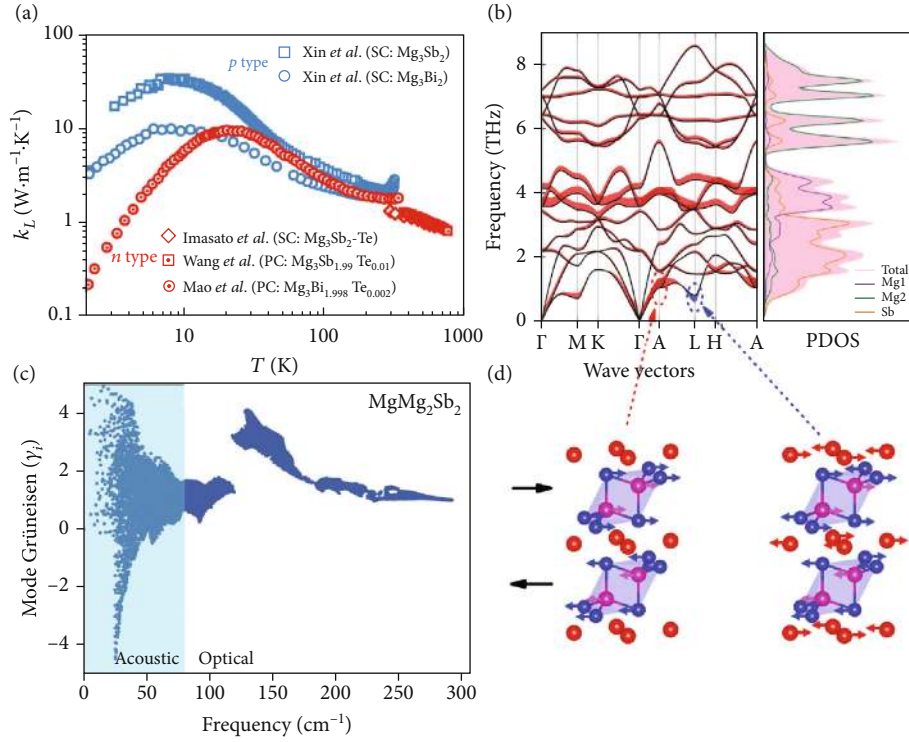
FIGURE 4: (a) The experimental κ_L of Mg_3X_2 and their alloys, where SC and PC denote single-crystalline and polycrystalline samples, respectively. The data are taken from Refs. [33, 96, 135, 142]. (b) Phonon dispersion and partial density of states (PDOS) of Mg_3Sb_2. (c) Mode Grüneisen parameter of Mg_3Sb_2. (d) The diagram of atomic displacement corresponding to the transverse at the A point (large positive γ_i) and at the L point (large negative γ_i). Panel (b) is reproduced with permission from Ref. [99]. CC-BY-4.0. Panels (c, d) are reproduced with permission from Ref. [94]. Copyright 2018 Elsevier Ltd.

A is a collection of physical constant, $\bar{M}$ the average mass of atoms of a crystal, θ_D the Debye temperature, δ^3 the volume per atom, N the number of atoms in the primitive unit cell, and γ the Grüneisen parameter reflecting the anharmonicity of the lattice [138]. The calculated γ for Mg_3Sb_2 is 1.83, which is higher than that of $CaMg_2Bi_2$ ($\gamma = 1.48$) and $CaMg_2Sb_2$ ($\gamma = 1.44$) having the same crystal structure [94]. The strong anharmonicity had also been confirmed by studying the κ_L of Mg_3X_2 using the Debye-Callaway model [135]. Comparatively, the other good TE materials with intrinsically low κ_L also show a large γ, such as PbTe (1.45) [139], $AgSbTe_2$ (2.05) [138], BiCuSeO (1.5) [140], MgAgSb (1.93) [59], and SnSe (3.13) [141].

The calculated mode Grüneisen parameter of Mg_3Sb_2 by Peng et al. [94] is presented in Figure 4(c). It is found that the phonons of Mg_3Sb_2 with frequency below 1 THz show both large positive and negative mode Grüneisen parameters, reflected by the red shadow at A point and blue shadow at L point, respectively. Both A and L points involve the shear movement of atoms in the ab-plane, as shown in Figure 4(d). More specifically, the same atoms in different layers move towards totally inverse direction at both A and L points, which could be one of the reasons for large shear stress between layers at these points [94]. Except for the large anharmonicity, Mg_3Sb_2 also shows a low sound velocity of $2587\,m\cdot s^{-1}$, while $CaMg_2Sb_2$ has an average sound velocity of $3317\,m\cdot s^{-1}$ [94], which also contributes to their low κ_L. Compared to Mg_3Sb_2, there is an obvious softening in the phonon density of states of Mg_3Bi_2 [143], owing to the heavier element Bi. This is why the κ_L of Mg_3Bi_2 is smaller than that of Mg_3Sb_2 [135].

Going further, there is still an interesting question concerning the thermal properties of Mg_3X_2. That is, why the large anharmonicity occurs in Mg_3X_2 but not in isoelectronic substituted $CaMg_2X_2$. Peng et al. [94] argued that the undersized Mg ions do not obey the octahedral bonding rules, leading to the instability of the octahedral site. Zhang et al. [99] thought that the higher formation enthalpy of Mg_3X_2 might lead to their relative instability and thus the soft mode and low κ_L. Because there are few experimental works focusing on the understanding of the phononic structure of Mg_3X_2 at present, future studies, for example, using inelastic phonon scattering [144, 145], might help to reveal the origin of large anharmonicity in Mg_3X_2.

The anisotropy of κ_L is also a worthy question requiring a detailed discussion. In the original work of Tamaki et al. [70], the sound velocities of longitudinal acoustic mode along the ab-plane and c-axis are calculated to be $4160\,m\cdot s^{-1}$ and $4730\,m\cdot s^{-1}$, respectively, from which they concluded a nearly isotropic character in thermal conduction of Mg_3Sb_2. This conclusion is further supported by the chemical bonding analysis by Zhang et al. [121] where they found that Mg_3Sb_2 exhibits a nearly isotropic three-dimensional bonding network with the interlayer and intralayer bonds being mostly

ionic and similar. The calculated κ_L along the *ab*-plane and *c*-axis is very close. Experimentally, Song et al. [146] prepared the texture-enhanced $Mg_3Sb_{2-x}Bi_x$ samples, from which they found that the lattice thermal conductivities are almost the same along the pressing direction and in-plane one. In short, the advantage of the nearly isotropic thermal and electrical conductions in *n*-type $Mg_3Sb_{2-x}Bi_x$ is that one does not need to specially take care of the direction of polycrystalline samples when doing the high-temperature thermal and electrical properties. This is actually not the case for the other layered TE materials, for example, Bi_2Te_3-based compounds, for which the zT can be overestimated if not measuring all the transport properties in the same direction [10, 147, 148].

3. Optimization of TE Properties

The chemical bonding, crystal, electronic, and phononic structures, discussed in the above section, lay the foundation for Mg_3X_2 as good thermoelectric materials. In practical experiments, the optimization of carrier concentration, engineering of the band and phononic structures, and regulation of electron and phonon scattering mechanisms are effective strategies to achieve high TE performance. Forming $Mg_3Sb_{2-x}Bi_x$ solid solutions is the most prevailing means to achieve a high zT (Figure 1). This is because Bi alloying could generate multiple beneficial effects, synergistically regulating both the electrical and thermal transport properties. Mg vacancy defects, which can directly affect the type of carriers, together with extrinsic chemical doping, are crucial for tuning the electrical transport properties of Mg_3X_2. Moreover, the electron scattering mechanism is another knob for achieving high electrical conductivity and good TE performance near RT. In this section, we focus on the discussions of Sb/Bi alloying, Mg vacancy defects, chemical doping, and carrier scattering mechanism, from which we will try to point out the ways towards high TE performance near RT.

3.1. Sb/Bi Alloying. Isoelectronic alloying to form solid solutions is a widely used strategy in TE research, of which the main purpose is to suppress the κ_L by introducing strong point defect scattering of phonons [149–151]. One key issue underlying the usage of this strategy is whether the solid solution can be formed in a full composition range (or whether there is a miscibility gap). The miscibility gap occurs in several TE systems, such as $Mg_2Si_{1-x}Sn_x$ [152–154], $Ti_{1-x}Zr_xNiSn$ [155, 156], and $Ti_{1-x}Zr_xCoSb$ [157, 158]. Luckily, there seems no miscibility gap in the $Mg_3Sb_{2-x}Bi_x$ system [33, 47, 73]. Intuitively, this can be understood partly from the mismatch in the lattice parameter of pristine compounds. For Mg_3Sb_2 and Mg_3Bi_2, the differences in the lattice parameter of both *a* and *c* directions are less than 2.5% (Table 1), while in the $Mg_2Si_{1-x}Sn_x$ system, the difference is larger than 6% [159]. This relatively smaller mismatch in the lattice parameter could to some extent explain the almost unaffected electron mobility of *n*-type $Mg_3Sb_{2-x}Bi_x$, which will be discussed in detail later together with the change of electronic structure.

Similar to the other TE solid solution systems, such as $PbTe_{1-x}Se_x$ [160], $Zr_{1-x}Hf_xNiSn$ [150], and $Zr_{1-x}Hf_xCoSb$ [159], the experimental κ_L for the $Mg_3Sb_{2-x}Bi_x$ system also presents a "U-shape" curve (Figure 5(a)), suggesting the efficacy in suppressing the lattice thermal transport with the enhanced point defect scattering of phonons. Near the pristine Mg_3Sb_2 and Mg_3Bi_2 sides, Bi/Sb alloying leads to a quick decay of κ_L, while in the region with $0.4 \le x \le 1.6$, the κ_L does not change obviously. Since the radius difference between Sb and Bi is relatively small, we tried to calculate the κ_L of the solid solution by only considering the mass fluctuation-induced point defect scattering of phonons [149]. As shown in Figure 5(a), the calculated line matches relatively well with the experimental results near the Mg_3Sb_2 side, indicating that the phonon scattering mainly comes from the mass fluctuation. Besides the effect of alloying on lattice thermal conductivity κ_L, the change of sound velocity, probably originating from the alloying-induced alternation of phonon dispersion, could also influence κ_L [161]. When alloying with Mg_3Bi_2, the sound velocity will decrease gradually from 2587 m/s of Mg_3Sb_2 to 2055 m/s of Mg_3Bi_2 [94, 143], indicating lattice softening and probably lower κ_L. This may be one of the reasons why the experimental results deviate from the calculated line in Figure 5(a). Additionally, there is a problem that needs to be paid attention to when comparing the κ_L and zT from different groups. Since $Mg_3Sb_{2-x}Bi_x$ alloy has been widely studied, the choices of heat capacity, either from the measurement or using the Dulong-Petit value, could to some extent influence the estimated κ_L and zT. Regarding this point, an empirical heat capacity equation was summarized by Agne et al. by including the Dulong-Petit value and temperature-dependent effects based on theory and experiment, which can be used without running C_p experiments on each sample: $C_p [\text{J} \cdot \text{g}^{-1} \cdot \text{K}^{-1}] = 3NR/M_w(1 + 1.3 \times 10^{-4} T - 4 \times 10^3 T^{-2})$ (for temperatures $200\,\text{K} \le T \le 800\,\text{K}$), where $3NR = 124.71\,\text{J} \cdot \text{mol}^{-1} \cdot \text{K}^{-1}$, M_w is the molecular weight of the formula unit being considered, and T is the absolute temperature [143]. To directly use this formula or take it as a standard reference for future studies is recommended so that a relatively fair comparison in the κ_L and zT can be reached.

In addition to the suppression of κ_L, there is also a tremendous change in the electronic structure of the $Mg_3Sb_{2-x}Bi_x$ system when changing *x* from 0 to 2 since Mg_3Sb_2 and Mg_3Bi_2 are semiconductor and semimetal, respectively (Figure 3(a)). This offers the opportunity to modulate the band structure of the $Mg_3Sb_{2-x}Bi_x$ solid solutions enabling desirable TE performance at different temperatures. Before going into the performance modulation, we first try to qualitatively understand the band structure evolution from Mg_3Sb_2 to Mg_3Bi_2 based on the molecular orbital analysis (Figure 5(b)). The valence electrons of Mg and Sb elements are 3*s* and 5*s*5*p*, respectively, mainly contributing to the formation of chemical bonding. The energy level of the Mg 3*s* orbital is higher than that of the Sb 5*p* orbital. When the Mg 3*s* and Sb 5*p* orbitals come together to form the two molecular orbitals, the upper antibonding state is mainly composed of the Mg 3*s* orbital while the lower bonding state mainly with Sb 5*p*. This real-space analysis of bonding formation can directly reflect the composition of the band
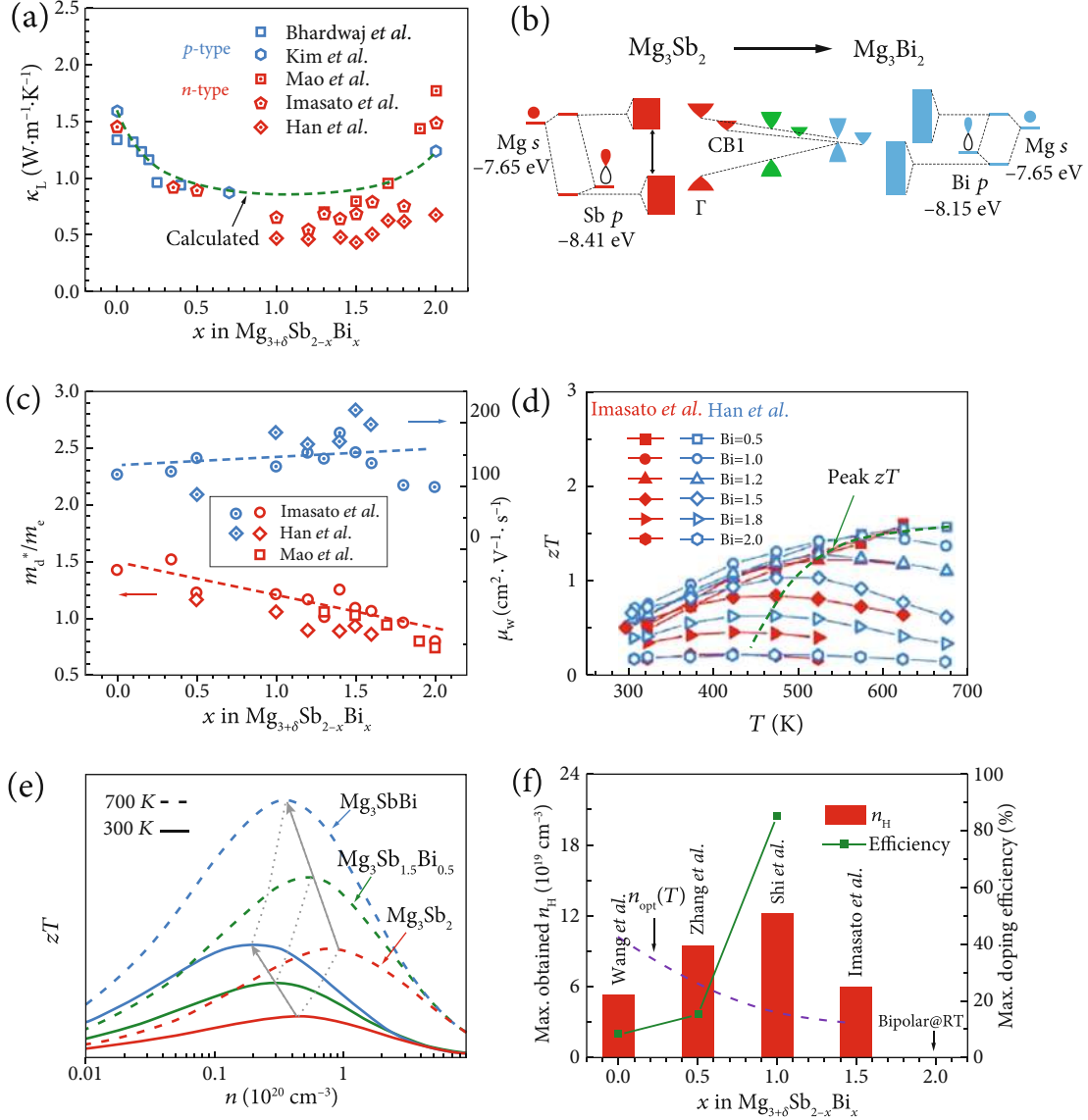
FIGURE 5: (a) κ_L at RT versus Bi alloying content for the $Mg_{3+\delta}Sb_{2-x}Bi_x$ system. The data are taken from Refs. [33, 47, 67, 68, 89]; the dashed line is modeled only considering the mass fluctuation-induced point defect scattering of phonons. (b) Schematic illustration of the hybridization in Mg_3X_2 and the evolution of band structure, inspired by the work of Zhang et al. and Pan et al. [48, 99]. These energies of valence atomic orbitals are taken from the Periodic Table of Atomic Orbital Energies [172]. (c) The density of states (DOS) effective mass and weighted mobility versus Bi content. The data are taken from Refs. [33, 47, 89]. (d) Temperature dependence of zT for the $Mg_{3+\delta}Sb_{2-x}Bi_x$ system with different Bi contents. The data are taken from Refs. [47, 89]. (e) Schematic carrier concentration dependence of zT for $Mg_3Sb_{2-x}Bi_x$ using the SPB model [164, 165]. (f) The experimentally obtained maximum Hall carrier concentration and the corresponding doping efficiency versus Bi content for the $Mg_{3+\delta}Sb_{2-x}Bi_x$ system. The purple dashed line indicates the estimated n_{opt} at 700 K obtained from Figure 5(e). The experimental data are taken from Refs. [47, 73, 118, 173].

structure in reciprocal space. As shown from the projected DOS analysis [127, 162, 163], the CBM is mainly contributed by the Mg s orbital while the Sb p orbital dominates the VBM. When the Sb atom is substituted by the Bi atom, it will lead to two main changes. On the one hand, the energy difference between the Mg 3s and Bi 6p orbitals is smaller than that between the Mg 3s and Sb 5p orbitals, leading to the reduced E_g in Mg_3Bi_2. On the other hand, the Bi 6p orbital is more dispersive than Sb 5p, which can further reduce the E_g and also result in lighter conduction and valence bands. These

qualitative analyses suggest that both E_g and conduction band effective mass will become smaller in the band evolution from Mg_3Sb_2 to Mg_3Bi_2.

Experimentally, the change in the density of state effective mass m_d^*, $m_d^* = N_v^{3/2} m_b^*$, which was derived from the measured S and n_H using the single parabolic band (SPB) model [164, 165], is presented in Figure 5(c), which indeed decreases with increasing Bi content. Moreover, the m_b^* obtained from the calculated electronic structure of the $Mg_3Sb_{2-x}Bi_x$ system was also reported by Han et al. [89],

exhibiting the same trend. Beneficial from the reduced m_b^*, the weighted mobility $\mu_w = \mu_0 (m_d^*/m_e)^{3/2}$ increases, where μ_0 is the mobility of a carrier at $k_B T$ higher than the band edge [166, 167]. Weighted mobility is also influenced by the scattering process when alloying with Bi. However, the alloying scattering is not so strong to decrease the carrier mobility. The reasons for this could be twofold: (i) the conduction band is dominated by the $3s$ states of Mg, and thus, the anion substitution does not significantly affect the conduction band transport, (ii) similar to what happens in the half-Heusler TE solid solutions [24, 159], where the small radius difference in the alloying and host atoms owing to lanthanide contraction does not induce a strong alloy scattering potential responsible for the negligible change in the carrier mobility. Hence, besides the suppressed κ_L, the weak alloy scattering of carriers and the reduced m_b^* are additional advantages for $Mg_3Sb_{2-x}Bi_x$ solid solutions to achieve better TE performance.

Going further, we now discuss the effect of the reduced E_g on the TE properties of $Mg_3Sb_{2-x}Bi_x$. In most of the previous TE studies, relatively large E_g, which can suppress the thermal excitation of minority carriers [3, 168], is generally desirable for obtaining a high peak zT at elevated temperatures. Since the possible TE applications of $Mg_3Sb_{2-x}Bi_x$ solid solutions are near RT, a too-large E_g is not really necessary as long as it can still effectively suppress the bipolar effect near RT. The optimum E_g of a TE material given by Sofo and Mahan is around 6–10 $k_B T$ [169], corresponding to 0.15–0.26 eV at 300 K. Figure 5(d) shows the temperature-dependent zT for n-type $Mg_3Sb_{2-x}Bi_x$ with different Bi contents [47, 89]. It is obvious to see that the temperature at which the peak zT occurs decreases with increasing Bi content. This gives an additional advantage for practical experiments. Namely, the optimal carrier concentration n_{opt} will become smaller (Figure 5(e)) and thus easier to be achieved experimentally [168, 170].

In short, Bi alloying in Mg_3Sb_2 has exhibited multiple beneficial effects on the TE properties. First, it can significantly suppress the phonon transport but weakly affect the carrier transport. Second, the lightened m_b^* contributes to higher μ_w. Third, the reduced E_g makes the n_{opt} easy to be achieved experimentally. Moreover, there is a large room to tune the peak zT of $Mg_3Sb_{2-x}Bi_x$ for applications at different temperatures. If aiming at power generation application, Sb-rich $Mg_3Sb_{2-x}Bi_x$ alloys have the advantage to achieve a high peak zT at elevated temperatures [70–73, 92]. However, owing to the solubility and efficiency of dopants, in the Sb-rich $Mg_3Sb_{2-x}Bi_x$ alloys, the experimentally maximum carrier concentration might still be lower than the n_{opt}, particularly for Mg_3Sb_2 (Figure 5(f)). Therefore, more efficient dopants are waiting to be found [171]. In contrast, to get high TE performance near RT, Bi-rich $Mg_3Sb_{2-x}Bi_x$ alloys with smaller E_g are enough, in which the smaller n_{opt} is easier to be reached, as recently demonstrated by Imasato et al. [47], Mao et al. [33], and Pan et al. [48].

3.2. Carrier Scattering Mechanism.
The carrier scattering mechanism is a very important aspect to understand the electrical transport of TE materials, which helps to find suitable

ways to improve TE performance by enhancing the carrier mobility and electrical conductivity. Since the discovery of n-type $Mg_3Sb_{2-x}Bi_x$ alloys [70, 71], an "anomalous" increase trend of $\mu(T)$ and $\sigma(T)$ near RT is frequently observed in the doped samples with small grain sizes (Figure 6(a)), which was initially explained as ionized impurity scattering [70, 72, 79, 85]. Ionized impurity scattering-dominated carrier transport is commonly observed in the lightly doped semiconductors near and below RT [174], which is quickly weakened with increasing carrier concentration that induces a strong screen of the ionized impurity centers [175]. That is why in most good TE materials (typically heavily doped semiconductors), the $\mu(T)$ and $\sigma(T)$ above RT generally decrease monotonously due to the dominated acoustic phonon scattering [176].

Back to n-type $Mg_3Sb_{2-x}Bi_x$ alloys, Kuo et al. [95] carefully analyzed the initially published experimental results and argued that the change from the ionized impurity scattering to acoustic phonon scattering near RT happens too fast to be satisfactorily explained by the conventional models using Matthiessen's rule. By considering the grain boundary region as an effectively separate phase rather than a scattering center, they put forward a two-phase model, which could successfully reproduce the experimentally observed $\sigma(T)$. Moreover, they predicted a large improvement in the room temperature zT if the grain boundary resistance is eliminated. Later, using atom probe tomography, the grain boundary phase is identified to be Mg-deficient (approximately 5 at%) (Figure 6(b)), which is attributed to be responsible for the high grain boundary resistance [98]. Aiming at improving the μ and σ near RT by suppressing the grain boundary resistance, one direct way is to simply reduce the number of grain boundaries to get coarse-grained polycrystalline samples, which can be achieved by either increasing the sintering temperature [78, 82] or post-annealing under Mg atmosphere if initial grain sizes are small [82]. Furthermore, melting followed by a sintering process has recently been reported as an effective way to prepare samples with large grain sizes [73, 92, 177]. Some experimental results also indicate that $Mg_3Sb_{2-x}Bi_x$ samples with high Bi content can have large grain sizes under the same preparing condition [47], which is probably due to their low melting points.

Beyond the coarse-grained polycrystalline samples, the prediction of Kuo et al. [95] directly points out that the single-crystalline $Mg_3Sb_{2-x}Bi_x$ samples could have the ceiling μ and σ near RT due to the almost-completely eliminated grain boundary resistance. In experiments, Imasato et al. [96] reported on the TE properties of n-type Te-doped Mg_3Sb_2 single crystals, synthesized by the Sb-flux method [135] and Mg-vapor annealing [82], of which the σ indeed exhibits a metallic behavior with a typical $T^{-1.5}$ dependence (Figure 6(a)), indicating the acoustic phonon scattering-dominated carrier transport and the absence of ionized impurity scattering [96]. Later, Pan et al. [48] reported on a direct growth of n-type Y-doped $Mg_3Sb_{0.75}Bi_{1.25}$ single crystals by the Mg-flux method, which exhibits a high zT of ~0.82 at 315 K that is comparable to the state-of-the-art n-type room temperature $Bi_2Te_{3-x}Se_x$-based TE alloys [8, 10, 147].

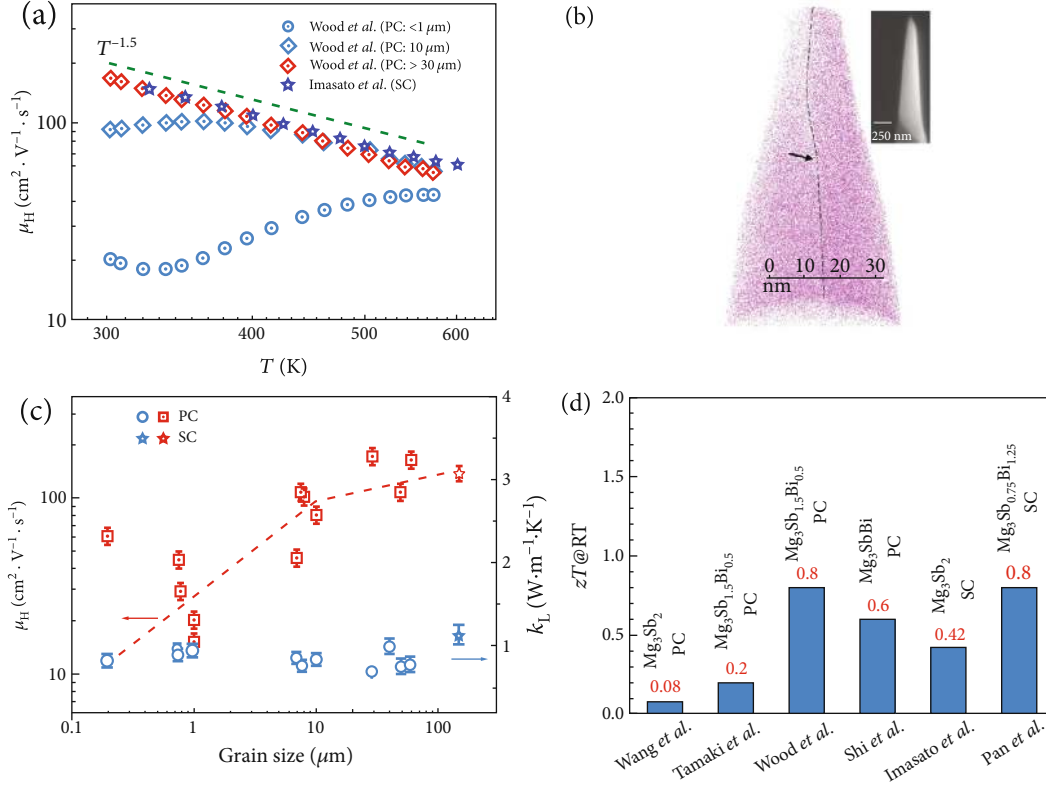FIGURE 6: (a) Temperature-dependent μ_H for $Mg_3Sb_{2-x}Bi_x$ synthesized with different grain sizes. The data are taken from Refs. [78, 82]. (b) 3D reconstruction of the atom distribution of the microtip of n-type Mg_3Sb_2. The upper-right inset is a scanning electron microscope image of the APT specimen. (c) The μ_H and κ_L at RT versus grain size for $Mg_3(Sb,Bi)_2$ solid solutions, adapted from Ref. [48] with the data taken from Refs. [33, 47, 48, 78, 79, 166, 178]. (d) zT at RT for SC and PC samples with different compositions and preparing methods. The data are taken from Refs. [48, 70, 73, 82, 96, 136]. Panel (b) is reproduced with permission from Ref. [98]. Copyright 2019 Wiley-VCH.

This series of work demonstrates a good research relay towards high-performance near-RT $Mg_3Sb_{2-x}Bi_x$ thermo-electrics based on the accurate understanding of the carrier scattering mechanism.

As extended discussions, we think there are another two points relating to this grain boundary resistance that are worth noting. On the one hand, the μ_H of polycrystalline samples at RT tends to have a slower increase when the grain size reaches above ~10 μm, while the κ_L only changes slightly with grain size (Figure 6(c)). Kuo et al. recently pointed out that there will be an overestimation of κ_L for small grain poly-crystalline samples because of high electrical resistance at the grain boundaries [179]. All of these indicate coarse-grained polycrystalline samples of tens of μm are preferred to have a similar TE performance to the single crystals with the same composition. As summarized in Figure 6(d), the coarse-grained samples and the single crystals indeed exhibit a close zT of approximately 0.8 at RT for $Mg_3Sb_{2-x}Bi_x$ solid solutions [48, 135]. Since the growth of centimeter-sized n-type single crystals is still challenging, coarse-grained polycrystalline samples could currently be preferable choice for practical applications.

On the other hand, it is the grain boundary phase which has a high resistance that leads to the "anomalous" $\mu(T)$ and $\sigma(T)$ near RT. Ideally, the grain boundary is thought of as a kind of very thin interface between two grains in a polycrys-talline material. However, in real materials, the grain bound-ary region could be more complicated than a thin interface due to the segregation of second phases or the change of composition [180, 181]. Good TE materials could particu-larly be the case since they always need to be alloyed or doped to tune the electrical and thermal properties for high perfor-mance, which unavoidably leads to complicated microstruc-tures [8, 182, 183]. Hence, a deep microstructure analysis to know the grain boundary region better with advanced tech-niques is highly necessary [184, 185]. For n-type Mg_3Sb_2 polycrystalline samples, the grain boundary phase is found to be a 10 nm region with Mg deficiency [98], resulting in the high electrical resistance. One possible indication thereby is if there are ways to make the grain boundary phase have an equal or even lower resistance than the matrix, the "anoma-lous" $\mu(T)$ and $\sigma(T)$ near RT might vanish. This might explain why in some experiments, even with the same prep-aration method, using highly metallic dopants or codoping, like Sc, Y, and some other transition metals, could to some extent tune the "anomalous" $\mu(T)$ and $\sigma(T)$ near RT [72, 85, 93]. The underlying reason might be that these highly metallic cation dopants make the grain boundary region have lower resistance compared to the less metallic anion dopants Te, Se, and S.
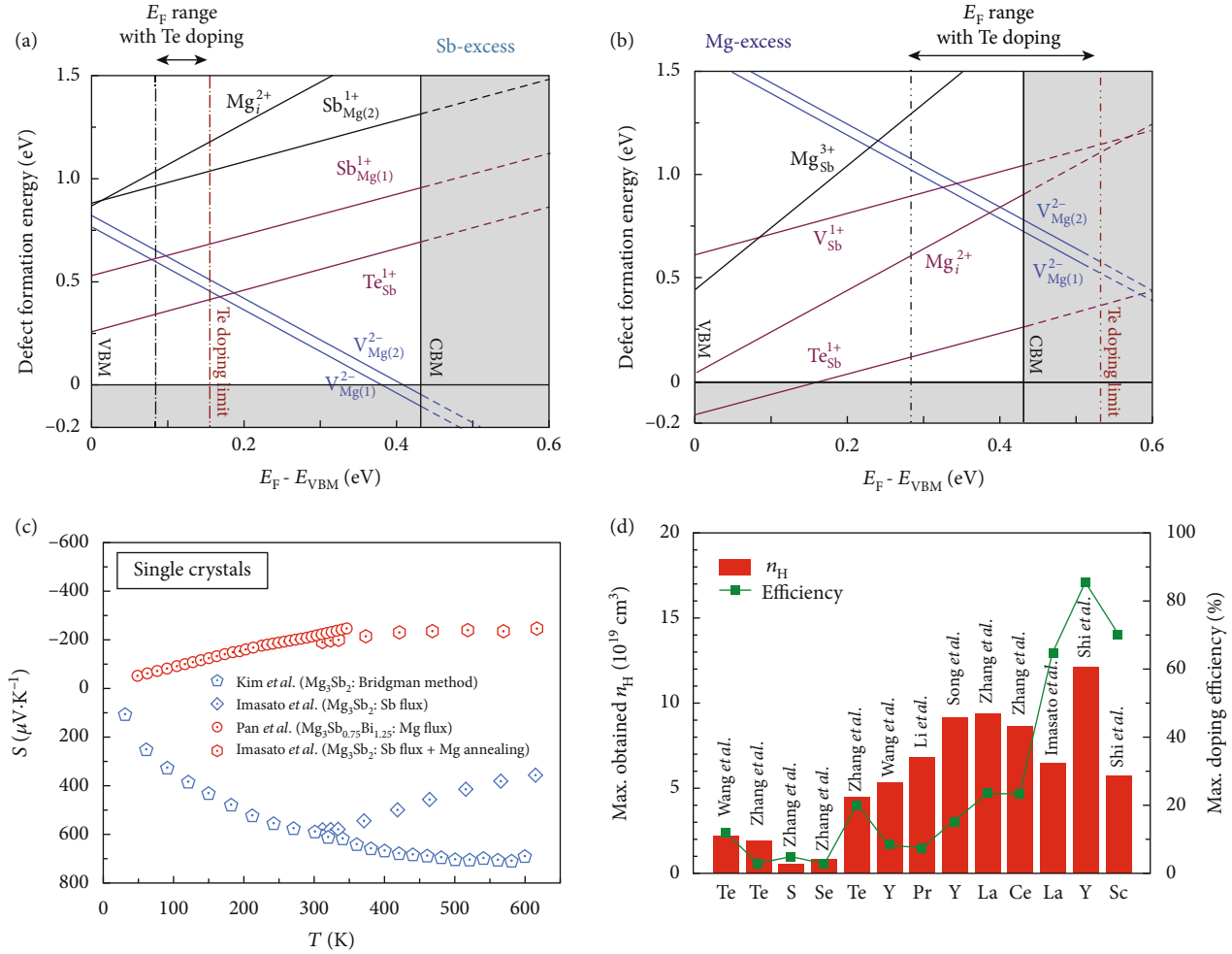
FIGURE 7: Defect formation energy in Mg_3Sb_2 in (a) Sb-excess and (b) Mg-excess conditions, respectively. (c) The Seebeck coefficient of Mg_3Sb_2 and $Mg_3(Sb,Bi)_2$ single crystals, grown under different chemical conditions. The data are taken from Refs. [48, 68, 96]. (d) The experimentally obtained maximum n_H in $Mg_3(Sb,Bi)_2$ samples and the calculated doping efficiency for different dopants. The blue color columns represent dopants at anion sites and the red at cation sites. The doping efficiency is calculated using the measured n_H divided by the theoretical one obtained assuming each doping atom offers one electron. The data are taken from Refs. [71, 73, 84, 86, 88, 92, 115, 118, 136, 173, 192, 193]. Panels (a, b) are reproduced with permission from Ref. [97]. Copyright 2018 Elsevier Ltd.

3.3. The Excess Mg and Chemical Doping. Intrinsic point defects, including vacancy, interstitial atoms, and antisite defects, could have important effects on both the electrical and thermal transport properties of TE materials [9, 186] and hence were studied extensively, such as Bi_{Te}^- antisite defect in Bi_2Te_3 [9, 187, 188], interstitial Ni in ZrNiSn [26, 189, 190], and Ag vacancy in MgAgSb [58, 191]. Mg vacancy and interstitial Mg are two commonly observed point defects in $Mg_2(Si,Ge,Sn)$-based TE materials [54, 55, 76], which could serve as acceptor and donor, respectively. For Mg_2Ge and Mg_2Sn, the type of carrier depends on the chemical environment of synthesis. A Mg-excess environment will lead to *n*-type transport behavior, while Mg deficiency to *p*-type [76]. For Mg_2Si, interstitial Mg is the dominant point defect in both Mg-excess and Mg-deficient environments, and hence, it always shows an *n*-type transport behavior [76].

Similarly, the $Mg_3Sb_{2-x}Bi_x$ system is also vitally affected by the chemical environment of synthesis [48, 70, 97]. To explore the dominant defect type, first-principles calculations

are commonly used to give a possible prediction [70, 97]. As shown in Figure 7(a), in the Sb-excess environment, Mg vacancy is the most stable defect near CBM. The *n*-doping by replacing Sb with Te fails to work since its formation energy is higher than that of Mg vacancy. Therefore, Te doping cannot shift the E_F into CBM if the chemical environment of synthesis is Sb-excess. In contrast, in the Mg-excess environment (Figure 7(b)), the formation energy of Mg vacancy is significantly increased, enabling the success of *n*-doping by substituting Te on the Sb site. Moreover, interstitial Mg has higher formation energy in both Sb-excess and Mg-excess conditions, indicating that only excess Mg in the synthesis process cannot help to shift the E_F into CBM.

Experimentally, the transport properties of single crystals grown from the liquid flux methods (Sb-excess and Mg-excess) match well the prediction of the defect calculations, as summarized in Figure 7(c). Mg_3Sb_2 single crystals synthesized by using the vertical Bridgman method [68] and Sb-flux method [135] show the transport behavior of an intrinsic

semiconductor with a large positive Seebeck coefficient. Te-doped Mg_3Sb_2 single crystals had also been successfully grown from the Sb-flux method, which however still shows the positive Seebeck coefficient, indicating Te doping itself cannot shift the E_F into CBM if the crystals are Mg-deficient [96]. Imasato et al. did a post-annealing of those Te-doped Mg_3Sb_2 single crystals under Mg-vapor, which successfully changed the transport behavior of the single crystals from p-type to n-type [96]. Very recently, using Mg as the flux, Pan et al. first reported a direct growth of Y-doped n-type Mg_3Sb_2 and $Mg_3Sb_{0.75}Bi_{1.25}$ single crystals [48]. Additionally, they found that the undoped Mg_3Sb_2 single crystal shows a weak p-type transport behavior despite grown out from the Mg-flux [48]. This suggests that interstitial Mg is difficult to enter into the lattice of Mg_3Sb_2, in agreement with the calculated phase diagram by Ohno et al. [97], where they found that the solubility of both excess Mg and Sb is less than 0.1%.

Excess Mg is then believed to be a prerequisite to obtain n-type $Mg_3Sb_{2-x}Bi_x$. One interesting question arises as to how much excess Mg should be added when synthesizing the polycrystalline samples. Both the defect calculations and single-crystal studies give a simple answer [48, 97]. That is, only slightly excess Mg (less than 0.1%) is necessary to guarantee the system to be n-type if efficient dopants are chosen [171, 195, 196]. However, for the experimental preparation of polycrystalline samples, the real conditions are more complicated. As highlighted in the very beginning, Mg is a very reactive element whose surface in the air will soon be covered by MgO. Moreover, in the mixture of raw elements and the high-temperature sintering process, Mg loss can happen and it varies with different milling methods (hand milling or ball milling) and different sintering temperatures and atmospheres. These make it very difficult to accurately control the content of excess Mg in practical experiments. As summarized in Table 3, excess Mg with a range from 0 to even as high as 16% had been used in the initial synthesis by different groups to compensate for the potential loss of Mg. However, since excess Mg is too difficult to enter into the lattice structure to form interstitial Mg defect [48, 97], adding too much excess Mg could result in the Mg-rich phase, as found by Shuai et al. [178]. In another experiment by Imasato et al. [87], they found that too much excess Mg could lead to an increase in the thermal conductivity and thus is detrimental for the overall TE performance. Moreover, too much excess Mg might also affect the stability of the synthesized polycrystalline samples, which will be discussed in the next section. It is worth noting that alloying Bi can lower the temperatures in either the melting or sintering process, which might be helpful to control the loss of Mg.

Under the Mg-excess condition, it is possible to achieve n-type $Mg_3Sb_{2-x}Bi_x$ by extrinsic doping. The selection of dopants is another key point determining the electrical performance of this TE material. Generally, several aspects need to be considered to find a good dopant: (i) whether a dopant enables the realization of n_{opt} since the doping efficiency varies for different elements; (ii) the dopant will induce defects or disorder in the host lattice, which may be detrimental to the carrier mobility. An empirical rule given by Ioffe that was summarized by Wang et al. [197] is as follows: the electron mobility is weakly affected if the dopant is introduced to the sub-lattice that has less contribution to the conduction band [197].

In the historical development of n-type $Mg_3Sb_{2-x}Bi_x$, the selection of dopants also follows such empirical criteria. Initially, the anion dopant Te was first selected to realize n-type transport [70, 71]. Subsequently, its isoelectronic chalcogen dopants S [86] and Se [84, 93] were also studied, which however are found to be less efficient due to the decreased carrier concentration and mobility [86]. Despite being the most efficient anion dopant, Te doping itself is difficult to realize the n_{opt} (up to 1×10^{20} cm^{-3}, Figure 5(e)) in Sb-rich $Mg_3Sb_{2-x}Bi_x$, owing to the limited solubility and doping efficiency (Figure 7(d)). The experimentally obtained maximum Hall carrier concentration is just 2×10^{19} cm^{-3} through Te doping at anion sites in Mg_3Sb_2 [136].

After the significant role of Mg-excess for realizing n-type doping was found [97], defect calculations predicted that Mg substitution with trivalent (or higher) cations can be even more effective than Se and Te doping to achieve high electron density above 1×10^{20} cm^{-3} [171, 195, 196]. In experiments, group 3 elements (Sc and Y) were found to be the most effective cation dopants which not only enable the realization of high carrier concentration (Figure 7(d)) but also have a weak effect on carrier transport [48, 73, 92, 173, 192]. The latter might originate from the smaller differences in the electronegativity and ionic radius between Mg and the dopants [86, 89, 159, 197]. The lanthanide dopants with a larger ionic radius, such as La, Pr, and Ce [115, 118, 193], were also found to be effective in achieving higher electron density than Te doping (Figure 7(d)) buthad an adverse effect on the carrier mobility. Moreover, the cation dopants on the Mg sites seem to have one more advantage than the anion dopants. That is, it can improve the thermal stability as will be discussed in the following section [73, 115].

4. TE Device and Thermal Stability

The rapid breakthrough in the TE performance of n-type $Mg_3Sb_{2-x}Bi_x$ from RT to 700 K ignited the research interest for practical device applications. Mao et al. [33] first reported on a unicouple consisting of n-type $Mg_{3.2}Bi_{1.498}Sb_{0.5}Te_{0.002}$ and p-type $Bi_{0.5}Sb_{1.5}Te_3$, as shown in the inset of Figure 8(a). When an input electrical current of 9 A is applied and the hot side is maintained at 350 K, the Peltier effect generated by this unicouple gives a maximum temperature difference of 91 K, which is even larger than the commercial Bi_2Te_3-based device [33]. This encouraging result suggests the potential of low-cost $Mg_3Sb_{2-x}Bi_x$ as a substitute for the current state-of-the-art n-type $Bi_2Te_{3-x}Se_x$. However, for practical device applications, there are still important engineering challenges awaiting further studies, including the design principle of the module, electrode fabrication, interface optimization, and protective coating [198–200]. The solutions to these engineering problems rely on the basic chemical and physical properties of $Mg_3Sb_{2-x}Bi_x$ alloys. Above all, the stability issues of $Mg_3Sb_{2-x}Bi_x$, including Mg loss and oxidization [65, 177], the decomposition and possible deterioration of TE performance [90, 91] at elevated

TABLE 3: The nominal element contents used by different groups to synthesize $Mg_3Sb_{2-x}Bi_x$ alloys. The preparation method, Hall carrier concentration, and peak zT are also shown. The data are taken from Refs. [33, 47, 48, 70–73, 80, 82, 84–88, 92, 93, 115, 192, 194].

| Nominal content | | Dopant | Method | n_H (10^{19} cm^{-3}) | zT | Reference |
Mg	Bi					
3.2	0.49	Te 0.01	BM+HP (Ar)	2	1.5@700 K	[70]
3	0.48	Te 0.04	AM+BM+SPS (Vac.)	2.2	1.65@725 K	[71]
3.07	0.48	Se 0.02	AM+BM+SPS (Vac.)	0.91	1.23@725 K	[84]
3.1	0.49	TM&Te 0.1&0.01	BM+HP	3-4.4	1.5-1.7@773 K	[72, 85]
3.2	0.49	Te 0.01	BM+HP	2.0-3.5	1.4-1.5@773 K	[192]
3	0.49	S 0.01	AM+BM+SPS (Vac.)	0.576	1.0@725 K	[86]
3.02	0.49-0.89	Mn&Te 0.01&0.01	BM+SPS	\	1.5-1.6@773 K	[80]
3.01-3.2	0.49	Te 0.01	BM+HP (Ar)	2.8-3.5	1.2-1.4@600 K	[87]
3.05	0.5	La 0.005	BM+HP (Ar)	5	1.0@600 K	[114]
3.2	0.49	Se 0.01	BM+HP	1.9	1.4@723 K	[93]
3.15	0.49	Mn&Se 0.05&0.01	BM+HP	2.1	1.7@623 K	[93]
3.032	1	Y 0.018	Melting+cut+HP	7.1	1.8@700 K	[73]
3.045	1	Sc 0.005	Melting+cut+HP	3.4	1.3@500 K	[92]
3.05	1.39825-1.393	Te 0.01	BM+HP (Ar)	2.3-6	1.0-1.2@400-500 K	[47]
3.02	0.5	Y 0.02	BM+HP	3.6	1.8@773 K	[88]
3.2	1.298-1.498	Te 0.002	BM+HP	1.4	0.9@350 K	[33]
3.5	0	Sc&Te 0.03&0.04	Powder mix+SPS	2	1.5@725 K	[190]
3.01	0.49	Te 0.01	BM+HP (Ar)+Mg-vapor annealing	2.8	0.8@300 K, 1.4@700 K	[82]
>3	1.25	Y \	Mg-flux	1.6	0.82@315 K	[48]

BM: ball milling; HP: hot pressing; AM: arc melting; SPS: spark plasma sintering; Vac.: vacuum; TM: transition metal.

temperatures, and possible deliquescence under humid environment, need to be well addressed before long-term usage.

The stability problems for Mg_3Sb_2 came into attention even in the very early publication by Condron et al. in 2006, in which the studied samples exhibited a p-type semiconducting behavior [65]. They found oxygen present at the grain boundaries of the hot-pressed Mg_3Sb_2 samples. Mg loss and oxidization were also observed at temperatures above 900 K. In the case of n-type $Mg_3Sb_{2-x}Bi_x$

alloys, the oxidization of Mg was also observed. Shi et al. have tried to grind the melted $Mg_3Sb_{2-x}Bi_x$ ingots into powders under different atmospheres before hot pressing [177]. They found that, if the powders were ground in the glove box with the inert atmosphere, the obtained pellets will show a relatively low level of oxidization. Moreover, Mg deficiency was found at the grain boundary region in the n-type Mg_3Sb_2 samples by Kuo et al. [98]. In a temperature-dependent powder X-ray diffraction
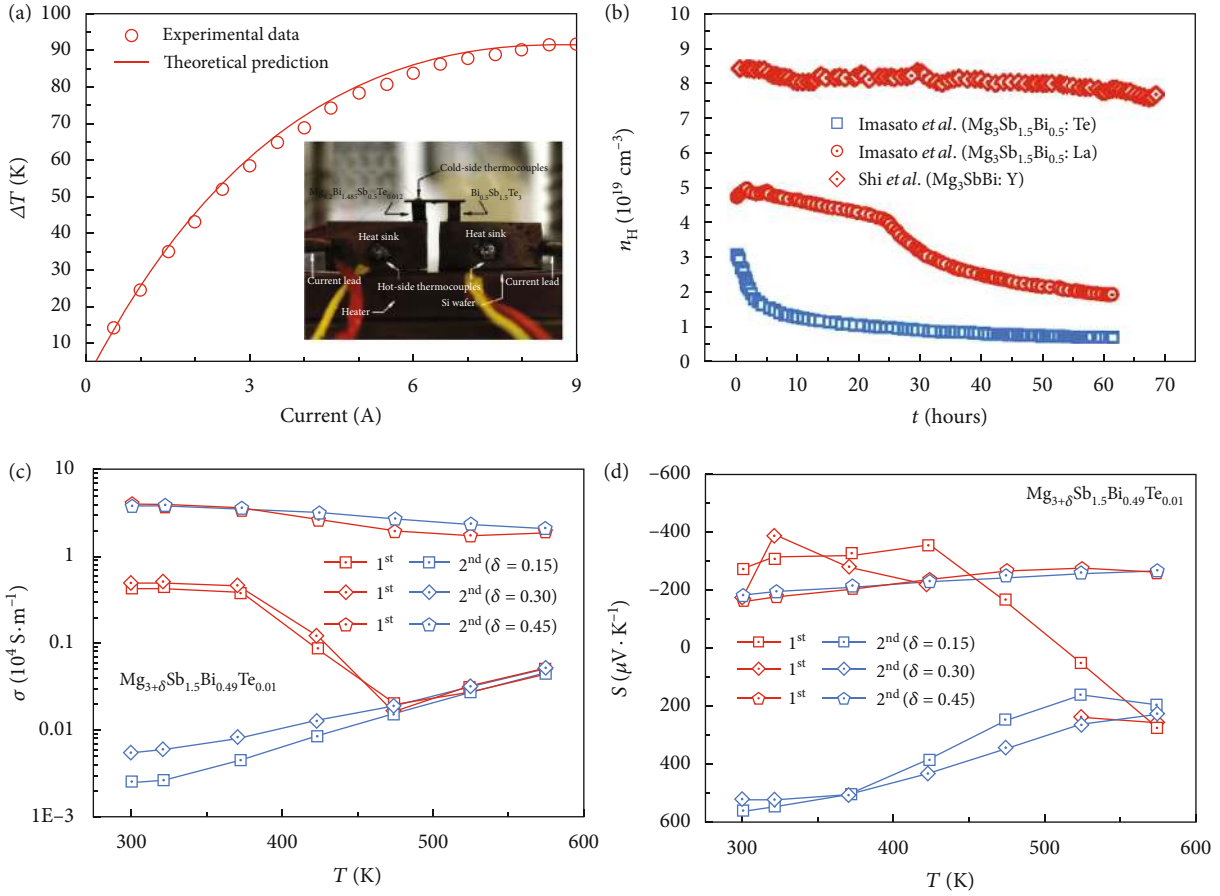
FIGURE 8: (a) Electrical current dependence of temperature difference (ΔT) between the hot and cold sides at the hot-side T of 350 K. The inset shows optical image of the experimental setup for the TE cooling measurement with a unicouple consisting of p-type $Bi_{0.5}Sb_{1.5}Te_3$ and n-type $Mg_{3.2}Bi_{1.498}Sb_{0.5}Te_{0.002}$. (b) Hall carrier concentration versus measurement time for La-doped samples under dynamic vacuum and Y-doped samples under vacuum; the data are taken from Refs. [73, 115]. (c, d) Temperature-dependent electrical conductivity and Seebeck coefficient of $Mg_{3+\delta}Sb_{1.5}Bi_{0.49}Te_{0.01}$ with different excess Mg in our experimental work. 1st and 2nd denote the first and second heating measurements in the helium atmosphere, respectively. Panel (a) is reproduced with permission from Ref. [33]. Copyright 2019 American Association for the Advancement of Science.

study, Song et al. [91] found that a secondary phase Sb appears even in the first heating process at temperatures above 500 K in both densified bulk samples and powdered samples of p-type $Mg_{2.985}Ag_{0.015}Sb_2$. A similar phenomenon also happened to n-type $Mg_3Sb_{1.475}Bi_{0.475}Te_{0.05}$, in which Jørgensen et al. found an approximately 11 wt.% of elemental bismuth crystallizing as a secondary phase after the first thermal cycle from 300 K to 725 K [90]. In another study by Chen et al. [79], a Bi-rich secondary phase was directly observed using TEM. Furthermore, Mao et al. [33] found that n-type $Mg_3Sb_{2-x}Bi_x$ in the air will deteriorate if Bi content is increased. This can be understood from the view of chemical bonding. Since the bond length of Mg-Bi is larger than that of Mg-Sb, the diminutive Mg1 atom will more severely deviate the octahedral rule with increasing Bi content in $Mg_3Sb_{2-x}Bi_x$ [94], making the interlayer bonding weaker and thus the thermal stability worse.

Luckily, the thermal stability of $Mg_3Sb_{2-x}Bi_x$ could be improved if suitable doping elements were chosen. Compared to doping at anion sites, some studies found that both donors and acceptors replacing Mg sites are beneficial for

improving the thermal stability, for example, doping Ag for p-type Mg_3Sb_2 [91] and Y [73], La [115], and Sc [92] for n-type $Mg_3Sb_{2-x}Bi_x$ (as shown in Figure 8(b)). This might be due to the larger sizes of these doping ions as the structural instability caused by the small size of Mg ions [97] can be improved after cationic doping. The thermal stability could also be improved by increasing nominal Mg content. Song et al. found that the Mg-excess p-type Mg_3Sb_2 show better stability than Mg-deficient ones [91]. We also checked the role of excess Mg on the electrical performance of Te-doped $Mg_{3+\delta}Sb_{2-x}Bi_x$ during thermal cycling in the helium atmosphere. As shown in Figures 8(c) and 8(d), the less Mg-excess samples show less stability than the more Mg-excess ones, and the former even show a change of the sign of the Seebeck coefficient during thermal cycling. The excess Mg is demanded to suppress the formation of Mg vacancies enabling n-type conduction and also better thermal stability. However, too much excess Mg, as discussed in the above section, will also lead to the oxidization and the increase of thermal conductivity [87], which might be detrimental for the long-term use of $Mg_{3+\delta}Sb_{2-x}Bi_x$ TE device.

All in all, it can be concluded that Mg plays a crucial role in the stability of this TE system. The small ionic radius of Mg makes it relatively unstable in the lattice of Mg_3X_2 [97], and Mg loss [70, 192] and the precipitation of the Sb/Bi phase [90, 91] can occur at elevated temperatures owing to the high vapor pressure of Mg. Luckily, doping at the Mg site could stabilize the lattice structure and balance the Mg loss [73, 115]. Considering that these problems are induced by the active Mg, the synthesis of $Mg_{3+\delta}Sb_{2-x}Bi_x$ materials and the assembly of TE devices need to control strictly the temperature and atmosphere to guarantee stability and reproducibility, particularly for practical applications. These might make the process cost of $Mg_{3+\delta}Sb_{2-x}Bi_x$ higher than that of Bi_2Te_3-based materials, although the cost of the raw elements in the former is lower. Moreover, for practical TE modules, there are additional demands for the exploration of matched p-type legs, suitable electrode materials, long-term interface stability, etc. All these aspects need to be comprehensively considered to finally answer the question of whether n-type $Mg_{3+\delta}Sb_{2-x}Bi_x$ can substitute $Bi_2Te_{3-x}Se_x$ for low-grade heat power generation and refrigeration.

5. Summary and Outlook

The past four years have witnessed the rapid development of n-type $Mg_3Sb_{2-x}Bi_x$ TE alloys with high zT values above 1.5 at 700 K and 0.8 at 300 K. These cheering results make low-cost $Mg_3Sb_{2-x}Bi_x$ a promising substitute for state-of-the-art n-type $Bi_2Te_{3-x}Se_x$ for power generation and refrigeration near RT. The reasons underlying the high TE performance are high band degeneracy and weighted mobility enabling large power factor and strong anharmonicity guaranteeing low lattice thermal conductivity. These good electrical and thermal transport properties are fundamentally determined by the intrinsic crystallographic, electronic, and phononic structures of Mg_3X_2 strongly linked to the element Mg. The interaction between the Mg1 and Mg2 atoms is a possible origin leading to the high conduction band degeneracy. The diminutive size of Mg, which is too small for the octahedrally coordinated site, leads to weak interlayer bonding and low thermal conductivity but also thermal instability. The close interactions of Mg1-Sb and Mg2-Sb are attributed to the nearly isotropic thermal properties. Moreover, only under the Mg-excess condition can n-type doping be realized for the $Mg_3Sb_{2-x}Bi_x$ system. However, active Mg also brings problems for both current laboratory research and future applications. That is, Mg loss and oxidation at elevated temperatures could lead to the decomposition of the compounds and deterioration of electrical performance.

With the deep understanding of band structure, the carrier scattering mechanism, and roles of cation dopants, the TE performance of n-type $Mg_3Sb_{2-x}Bi_x$ is already comparable to that of the state-of-the-art $Bi_2Te_{3-x}Se_x$, laying a good foundation for practical TE applications near RT. Further studies on device design and fabrication are now calling on. In the meantime, the thermal and chemical stabilities of n-type $Mg_3Sb_{2-x}Bi_x$ alloys, which are strongly related to the active Mg element, will bring real challenges. All the processes, including material synthesis, transfer, joint connection, module assembly, and packaging, might need to be strictly controlled. Suitable interface materials, mechanical property tests, and large-scale production of TE modules are awaiting further studies. Moreover, despite the currently developed unicouple, $Mg_3Sb_{2-x}Bi_x$ and $Bi_{2-x}Sb_xTe_3$ as the n-type and p-type legs, respectively, give a very promising cooling performance, and whether $Bi_{2-x}Sb_xTe_3$ is the best p-type material for multipair TE module still needs further studies. The exploration of matched p-type material, based on $Mg_3Sb_{2-x}Bi_x$ or the other isoelectronic Zintl phase, should be put on the agenda.

Conflicts of Interest

The authors declare no conflicts of interest.

Authors' Contributions

A. Li collected and analyzed the data, did the investigation, and wrote the original draft; C. Fu, X. Zhao, and T. Zhu conceived the idea and reviewed and edited the manuscript.

Acknowledgments

References

[1] J. He and T. M. Tritt, "Advances in thermoelectric materials research: looking back and moving forward," *Science*, vol. 357, no. 6358, p. eaak9997, 2017.

[2] G. J. Snyder and E. S. Toberer, "Complex thermoelectric materials," *Nature Materials*, vol. 7, no. 2, pp. 105–114, 2008.

[3] Y. Pei, H. Wang, and G. J. Snyder, "Band engineering of thermoelectric materials," *Advanced Materials*, vol. 24, no. 46, pp. 6125–6135, 2012.

[4] T. Zhu, Y. Liu, C. Fu, J. P. Heremans, J. G. Snyder, and X. Zhao, "Compromise and synergy in high-efficiency thermoelectric materials," *Advanced Materials*, vol. 29, no. 14, Article ID 1605884, 2017.

[5] J. Yang, L. Xi, W. Qiu et al., "On the tuning of electrical and thermal transport in thermoelectrics: an integrated theory–experiment perspective," *NPJ Computational Materials*, vol. 2, no. 1, Article ID 15015, 2016.

[6] P. Gorai, V. Stevanović, and E. S. Toberer, "Computationally guided discovery of thermoelectric materials," *Nature Reviews Materials*, vol. 2, no. 9, Article ID 17053, 2017.

[7] B. Poudel, Q. Hao, Y. Ma et al., "High-thermoelectric performance of nanostructured bismuth antimony telluride bulk alloys," *Science*, vol. 320, no. 5876, pp. 634–638, 2008.

[8] L. Hu, H. Wu, T. Zhu et al., "Tuning multiscale microstructures to enhance thermoelectric performance of n-type bismuth-telluride-based solid solutions," *Advanced Energy Materials*, vol. 5, no. 17, Article ID 1500411, 2015.

[9] T. Zhu, L. Hu, X. Zhao, and J. He, "New insights into intrinsic point defects in V2VI3Thermoelectric materials," *Advanced Science*, vol. 3, no. 7, Article ID 1600004, 2016.

[10] Y. Pan, Y. Qiu, I. Witting et al., "Synergistic modulation of mobility and thermal conductivity in $(Bi,Sb)_2Te_3$ towards high thermoelectric performance," *Energy & Environmental Science*, vol. 12, no. 2, pp. 624–630, 2019.

[11] Y. Pei, X. Shi, A. LaLonde, H. Wang, L. Chen, and G. J. Snyder, "Convergence of electronic bands for high performance bulk thermoelectrics," *Nature*, vol. 473, no. 7345, pp. 66–69, 2011.

[12] H. Wang, Y. Pei, A. D. LaLonde, and G. J. Snyder, "Weak electron–phonon coupling contributing to high thermoelectric performance in n-type PbSe," *Proceedings of the National Academy of Sciences*, vol. 109, no. 25, pp. 9705–9709, 2012.

[13] K. Biswas, J. He, I. D. Blum et al., "High-performance bulk thermoelectrics with all-scale hierarchical architectures," *Nature*, vol. 489, no. 7416, pp. 414–418, 2012.

[14] H. Wang, Z. M. Gibbs, Y. Takagiwa, and G. J. Snyder, "Tuning bands of PbSe for better thermoelectric efficiency," *Energy & Environmental Science*, vol. 7, no. 2, pp. 804–811, 2014.

[15] L.-D. Zhao, G. Tan, S. Hao et al., "Ultrahigh power factor and thermoelectric performance in hole-doped single-crystal SnSe," *Science*, vol. 351, no. 6269, pp. 141–144, 2016.

[16] C. Chang, M. Wu, D. He et al., "3D charge and 2D phonon transports leading to high out-of-planeZTin n-type SnSe crystals," *Science*, vol. 360, no. 6390, pp. 778–783, 2018.

[17] M. Hong, J. Zou, and Z.-G. Chen, "Thermoelectric GeTe with diverse degrees of freedom having secured superhigh performance," *Advanced Materials*, vol. 31, no. 14, p. 1807071, 2019.

[18] X. Zhang, Z. Bu, S. Lin, Z. Chen, W. Li, and Y. Pei, "GeTe Thermoelectrics," *Joule*, vol. 4, no. 5, pp. 986–1003, 2020.

[19] H. Liu, X. Shi, F. Xu et al., "Copper ion liquid-like thermoelectrics," *Nature Materials*, vol. 11, no. 5, pp. 422–425, 2012.

[20] Y. He, T. Day, T. Zhang et al., "High thermoelectric performance in non-toxic earth-abundant copper sulfide," *Advanced Materials*, vol. 26, no. 23, pp. 3974–3978, 2014.

[21] C. Fu, T. Zhu, Y. Pei et al., "High band degeneracy contributes to high thermoelectric performance in p-type half-Heusler compounds," *Advanced Energy Materials*, vol. 4, no. 18, Article ID 1400600, 2014.

[22] C. Fu, S. Bai, Y. Liu et al., "Realizing high figure of merit in heavy-band p-type half-Heusler thermoelectric materials," *Nature Communications*, vol. 6, no. 1, Article ID 8144, 2015.

[23] T. Zhu, C. Fu, H. Xie, Y. Liu, and X. Zhao, "High efficiency half-Heusler thermoelectric materials for energy harvesting," *Advanced Energy Materials*, vol. 5, no. 19, Article ID 1500588, 2015.

[24] J. Yu, C. Fu, Y. Liu et al., "Unique role of refractory Ta alloying in enhancing the figure of merit of NbFeSb thermoelectric materials," *Advanced Energy Materials*, vol. 8, no. 1, Article ID 1701313, 2018.

[25] H. Zhu, J. Mao, Y. Li et al., "Discovery of TaFeSb-based half-Heuslers with high thermoelectric performance," *Nature Communications*, vol. 10, no. 1, p. 270, 2019.

[26] C. Fu, M. Yao, X. Chen et al., "Revealing the intrinsic electronic structure of 3D half-Heusler thermoelectric materials by angle-resolved photoemission spectroscopy," *Advanced Science*, vol. 7, no. 1, Article ID 1902409, 2020.

[27] X. Shi, J. Yang, J. R. Salvador et al., "Multiple-filled skutterudites: high thermoelectric figure of merit through separately optimizing electrical and thermal transports," *Journal of the American Chemical Society*, vol. 133, no. 20, pp. 7837–7846, 2011.

[28] Y. Tang, Z. M. Gibbs, L. A. Agapito et al., "Convergence of multi-valley bands as the electronic origin of high thermoelectric performance in $CoSb_3$ skutterudites," *Nature Materials*, vol. 14, no. 12, pp. 1223–1228, 2015.

[29] W. Zhao, Z. Liu, Z. Sun et al., "Superparamagnetic enhancement of thermoelectric performance," *Nature*, vol. 549, no. 7671, pp. 247–251, 2017.

[30] T. Caillat, J. P. Fleurial, and A. Borshchevsky, "Preparation and thermoelectric properties of semiconducting Zn_4Sb_3," *Journal of Physics and Chemistry of Solids*, vol. 58, no. 7, pp. 1119–1125, 1997.

[31] G. J. Snyder, M. Christensen, E. Nishibori, T. Caillat, and B. B. Iversen, "Disordered zinc in Zn_4Sb_3 with phonon-glass and electron-crystal thermoelectric properties," *Nature Materials*, vol. 3, no. 7, pp. 458–463, 2004.

[32] S. R. Brown, S. M. Kauzlarich, F. Gascoin, and G. J. Snyder, "$Yb_{14}MnSb_{11}$: new high efficiency thermoelectric material for power generation," *Chemistry of Materials*, vol. 18, no. 7, pp. 1873–1877, 2006.

[33] J. Mao, H. Zhu, Z. Ding et al., "High thermoelectric cooling performance of n-type Mg_3Bi_2-based materials," *Science*, vol. 365, no. 6452, pp. 495–498, 2019.

[34] X. Shi, J. Yang, S. Bai et al., "On the design of high-efficiency thermoelectric clathrates through a systematic cross-substitution of framework elements," *Advanced Functional Materials*, vol. 20, no. 5, pp. 755–763, 2010.

[35] T. Takabatake, K. Suekuni, T. Nakayama, and E. Kaneshita, "Phonon-glass electron-crystal thermoelectric clathrates: experiments and theory," *Reviews of Modern Physics*, vol. 86, no. 2, pp. 669–716, 2014.

[36] W. Liu, X. Tan, K. Yin et al., "Convergence of conduction bands as a means of enhancing thermoelectric performance ofn-TypeMg$_2$Si$_{1-x}$Sn$_x$ Solid solutions," *Physical Review Letters*, vol. 108, no. 16, article 166601, 2012.

[37] W. Liu, H. S. Kim, S. Chen et al., "n-Type Thermoelectric Material $Mg_2Sn_{0.75}Ge_{0.25}$ for High Power Generation," *Proceedings of the National Academy of Sciences*, vol. 112, no. 11, pp. 3269–3274, 2015.

[38] X. Chen, A. Weathers, J. Carrete et al., "Twisting phonons in complex crystals with quasi-one-dimensional substructures," *Nature Communications*, vol. 6, no. 1, Article ID 6723, 2015.

[39] G. Joshi, H. Lee, Y. Lan et al., "Enhanced thermoelectric figure-of-merit in nanostructured p-type silicon germanium bulk alloys," *Nano Letters*, vol. 8, no. 12, pp. 4670–4674, 2008.

[40] B. Yu, M. Zebarjadi, H. Wang et al., "Enhancement of thermoelectric properties by modulation-doping in silicon germanium alloy nanocomposites," *Nano Letters*, vol. 12, no. 4, pp. 2077–2082, 2012.

[41] "Solid-state cooling market by product, type, end-user industry, region- Global Forecast to 2024," June 2020, https://www.reportlinker.com/p05804676/Solid-State-Cooling-Market-

by-Product-Type-End-User-Industry-Region-Global-Forecast-to.html?utm_source=GNW.

[42] A. F. Ioffe, L. S. Stil'bans, E. K. Iordanishvili, T. S. Stavitskaya, A. Gelbtuch, and G. Vineyard, "Semiconductor thermoelements and thermoelectric cooling," *Physics Today*, vol. 12, no. 5, p. 42, 1959.

[43] J. P. Heremans, R. J. Cava, and N. Samarth, "Tetradymites as thermoelectrics and topological insulators," *Nature Reviews Materials*, vol. 2, no. 10, Article ID 17049, 2017.

[44] M. J. Kirkham, A. M. dos Santos, C. J. Rawn, E. Lara-Curzio, J. W. Sharp, and A. J. Thompson, "Abinitiodetermination of crystal structures of the thermoelectric material MgAgSb," *Physical Review B*, vol. 85, no. 14, Article ID 144120, 2012.

[45] H. Zhao, J. Sui, Z. Tang et al., "High thermoelectric performance of MgAgSb-based materials," *Nano Energy*, vol. 7, pp. 97–103, 2014.

[46] P. Ying, X. Liu, C. Fu et al., "High performance α-MgAgSb thermoelectric materials for low temperature power generation," *Chemistry of Materials*, vol. 27, no. 3, pp. 909–913, 2015.

[47] K. Imasato, S. D. Kang, and G. J. Snyder, "Exceptional thermoelectric performance in $Mg_3Sb_{0.6}Bi_{1.4}$ for low-grade waste heat recovery," *Energy & Environmental Science*, vol. 12, no. 3, pp. 965–971, 2019.

[48] Y. Pan, M. Yao, X. Hong et al., "$Mg_3(Bi,Sb)_2$ single crystals towards high thermoelectric performance," *Energy & Environmental Science*, vol. 13, no. 6, pp. 1717–1724, 2020.

[49] D. R. Lidde, *CRC Handbook of Chemistry and Physics*, Taylor & Francis Group, 89th edition, 2008.

[50] E. N. Nikitin, "Thermoelectric properties of solid solutions Mg_2Si-Mg_2Sn," *Soviet Physics-Solid State*, vol. 3, p. 2648, 1962.

[51] V. K. Zaitsev, M. I. Fedorov, E. A. Gurieva et al., "Highly effective $Mg_2Si_{1-x}Sn_x$ thermoelectrics," *Physical Review B*, vol. 74, no. 4, Article ID 045207, 2006.

[52] W. Liu, J. Zhou, Q. Jie et al., "New insight into the material parameter B to understand the enhanced thermoelectric performance of $Mg_2Sn_{1-x-y}Ge_xSb_y$," *Energy & Environmental Science*, vol. 9, no. 2, pp. 530–539, 2016.

[53] W. Liu, K. Yin, Q. Zhang, C. Uher, and X. Tang, "Eco-friendly high-performance silicide thermoelectric materials," *National Science Review*, vol. 4, no. 4, pp. 611–626, 2017.

[54] G. Jiang, J. He, T. Zhu et al., "High performance $Mg_2(Si,Sn)$ solid solutions: a point defect chemistry approach to enhancing thermoelectric properties," *Advanced Functional Materials*, vol. 24, no. 24, pp. 3776–3781, 2014.

[55] J. Xin, H. Wu, X. Liu, T. Zhu, G. Yu, and X. Zhao, "Mg vacancy and dislocation strains as strong phonon scatterers in $Mg_2Si_{1-x}Sb_x$ thermoelectric materials," *Nano Energy*, vol. 34, pp. 428–436, 2017.

[56] W. S. H. Nowotny, "Ternäre Valenzverbindungen in den Systemen Kupfer (Silber)-Arsen (Antimon, Wismut)-Magnesium," *Zeitschrift für Metallkunde*, vol. 33, pp. 391–394, 1941.

[57] Z. Liu, W. Gao, X. Meng et al., "Mechanical properties of nanostructured thermoelectric materials α-MgAgSb," *Scripta Materialia*, vol. 127, pp. 72–75, 2017.

[58] Z. Liu, J. Mao, J. Sui, and Z. Ren, "High thermoelectric performance of α-MgAgSb for power generation," *Energy & Environmental Science*, vol. 11, no. 1, pp. 23–44, 2018.

[59] P. Ying, X. Li, Y. Wang et al., "Hierarchical chemical bonds contributing to the intrinsically low thermal conductivity in

α-MgAgSb thermoelectric materials," *Advanced Functional Materials*, vol. 27, no. 1, Article ID 1604145, 2017.

[60] J.-L. Mi, P.-J. Ying, M. Sist et al., "Elaborating the crystal structures of MgAgSb thermoelectric compound: polymorphs and atomic disorders," *Chemistry of Materials*, vol. 29, no. 15, pp. 6378–6388, 2017.

[61] E. Zintl and E. Husemann, "Bindungsart und Gitterbau binärer Magnesiumverbindungen," *Zeitschrift für physikalische Chemie*, vol. 21B, no. 1, pp. 138–155, 1933.

[62] H. Schäfer, B. Eisenmann, and W. Müller, "Zintl phases: transitions between metallic and ionic bonding," *Angewandte Chemie International Edition in English*, vol. 12, no. 9, pp. 694–712, 1973.

[63] L. Pincherle and J. M. Radcliffe, "Semiconducting intermetallic compounds," *Advances in Physics*, vol. 5, no. 19, pp. 271–322, 1956.

[64] T. Kajikawa, N. Kimura, and T. Yokoyama, "Thermoelectric properties of intermetallic compounds: Mg_3Bi_2 and Mg_3Sb_2 for medium temperature range thermoelectric elements," in *22nd International Conference on Thermoelectrics (ICT)*, pp. 305–308, La Grande Motte, France, August 2003.

[65] C. L. Condron, S. M. Kauzlarich, F. Gascoin, and G. J. Snyder, "Thermoelectric properties and microstructure of Mg_3Sb_2," *Journal of Solid State Chemistry*, vol. 179, no. 8, pp. 2252–2257, 2006.

[66] H. X. Xin and X. Y. Qin, "Electrical and thermoelectric properties of nanocrystal substitutional semiconductor alloys $Mg_3(Bi_xSb_{1-x})_2$ prepared by mechanical alloying," *Journal of Physics D: Applied Physics*, vol. 39, no. 24, pp. 5331–5337, 2006.

[67] A. Bhardwaj, A. Rajput, A. K. Shukla et al., "Mg_3Sb_2-based Zintl compound: a non-toxic, inexpensive and abundant thermoelectric material for power generation," *RSC Advances*, vol. 3, no. 22, pp. 8504–8516, 2013.

[68] S. Kim, C. Kim, Y.-K. Hong et al., "Thermoelectric properties of Mn-doped Mg–Sb single crystals," *Journal of Materials Chemistry A*, vol. 2, no. 31, pp. 12311–12316, 2014.

[69] J. Shuai, Y. Wang, H. S. Kim et al., "Thermoelectric properties of Na-doped Zintl compound: $Mg_{3-x}Na_xSb2$," *Acta Materialia*, vol. 93, pp. 187–193, 2015.

[70] H. Tamaki, H. K. Sato, and T. Kanno, "Isotropic conduction network and defect chemistry in $Mg_{3+\delta}Sb_2$-based layered Zintl compounds with high thermoelectric performance," *Advanced Materials*, vol. 28, no. 46, pp. 10182–10187, 2016.

[71] J. Zhang, L. Song, S. H. Pedersen, H. Yin, L. T. Hung, and B. B. Iversen, "Discovery of high-performance low-cost *n*-type Mg_3Sb_2-based thermoelectric materials with multivalley conduction bands," *Nature Communications*, vol. 8, no. 1, Article ID 13901, 2017.

[72] J. Shuai, J. Mao, S. Song et al., "Tuning the carrier scattering mechanism to effectively improve the thermoelectric properties," *Energy & Environmental Science*, vol. 10, no. 3, pp. 799–807, 2017.

[73] X. Shi, T. Zhao, X. Zhang et al., "Extraordinary *n*-type Mg_3SbBi thermoelectrics enabled by yttrium doping," *Advanced Materials*, vol. 31, no. 36, Article ID 1903387, 2019.

[74] P. Gorai, A. Ganose, A. Faghaninia, A. Jain, and V. Stevanović, "Computational discovery of promising new *n*-type dopable ABX Zintl thermoelectric materials," *Materials Horizons*, vol. 7, no. 7, pp. 1809–1818, 2020.

[75] W. Liu, X. Tang, H. Li, J. Sharp, X. Zhou, and C. Uher, "Optimized thermoelectric properties of Sb-doped $Mg_{2(1+z)}Si_{0.5-}$

$_y$Sn$_{0.5}$Sb$_y$ through adjustment of the Mg content," *Chemistry of Materials*, vol. 23, no. 23, pp. 5256–5263, 2011.

[76] X. Liu, L. Xi, W. Qiu et al., "Significant roles of intrinsic point defects in Mg$_2$X (X = Si, Ge, Sn) thermoelectric materials," *Advanced Electronic Materials*, vol. 2, no. 2, Article ID 1500284, 2016.

[77] L. Song, J. Zhang, and B. B. Iversen, "Simultaneous improvement of power factor and thermal conductivity via Ag doping in *p*-type Mg$_3$Sb$_2$ thermoelectric materials," *Journal of Materials Chemistry A*, vol. 5, no. 10, pp. 4932–4939, 2017.

[78] T. Kanno, H. Tamaki, H. K. Sato et al., "Enhancement of average thermoelectric figure of merit by increasing the grain-size of Mg$_{3.2}$Sb$_{1.5}$Bi$_{0.49}$Te$_{0.01}$," *Applied Physics Letters*, vol. 112, no. 3, Article ID 033903, 2018.

[79] X. Chen, H. Wu, J. Cui et al., "Extraordinary thermoelectric performance in *n*-type manganese doped Mg$_3$Sb$_2$ Zintl: high band degeneracy, tuned carrier scattering mechanism and hierarchical microstructure," *Nano Energy*, vol. 52, pp. 246–255, 2018.

[80] R. Shu, Y. Zhou, Q. Wang et al., "Mg$_{3+\delta}$Sb$_x$Bi$_{2-x}$ Family: a promising substitute for the state-of-the-art *n*-type thermoelectric materials near room temperature," *Advanced Functional Materials*, vol. 29, no. 4, Article ID 1807235, 2019.

[81] Z. Ren, J. Shuai, J. Mao et al., "Significantly enhanced thermoelectric properties of *p*-type Mg$_3$Sb$_2$ via co-doping of Na and Zn," *Acta Materialia*, vol. 143, pp. 265–271, 2018.

[82] M. Wood, J. J. Kuo, K. Imasato, and G. J. Snyder, "Improvement of Low-Temperature zT in a Mg$_3$Sb$_2$_Mg$_3$Bi$_2$ Solid solution via Mg-vapor annealing," *Advanced Materials*, vol. 31, no. 35, Article ID 1902337, 2019.

[83] X. Tang, B. Zhang, X. Zhang et al., "Enhancing the thermoelectric performance of *p*-type Mg$_3$Sb$_2$ via codoping of Li and Cd," *ACS Applied Materials & Interfaces*, vol. 12, no. 7, pp. 8359–8365, 2020.

[84] J. Zhang, L. Song, A. Mamakhel, M. R. V. Jørgensen, and B. B. Iversen, "High-performance low-cost *n*-type se-doped Mg$_3$Sb$_2$-based Zintl compounds for thermoelectric application," *Chemistry of Materials*, vol. 29, no. 12, pp. 5371–5383, 2017.

[85] J. Mao, J. Shuai, S. Song et al., "Manipulation of ionized impurity scattering for achieving high thermoelectric performance in *n*-type Mg$_3$Sb$_2$-based materials," *Proceedings of the National Academy of Sciences*, vol. 114, no. 40, pp. 10548–10553, 2017.

[86] J. Zhang, L. Song, K. A. Borup, M. R. V. Jørgensen, and B. B. Iversen, "New insight on tuning electrical transport properties via chalcogen doping in *n*-type Mg$_3$Sb$_2$-based thermoelectric materials," *Advanced Energy Materials*, vol. 8, no. 16, Article ID 1702776, 2018.

[87] K. Imasato, S. Ohno, S. D. Kang, and G. J. Snyder, "Improving the thermoelectric performance in Mg$_{3+x}$Sb$_{1.5}$Bi$_{0.49}$Te$_{0.01}$ by reducing excess Mg," *APL Materials*, vol. 6, no. 1, Article ID 016106, 2018.

[88] S. W. Song, J. Mao, M. Bordelon et al., "Joint effect of magnesium and yttrium on enhancing thermoelectric properties of *n*-type Zintl Mg$_{3+\delta}$Y$_{0.02}$Sb$_{1.5}$Bi$_{0.5}$," *Materials Today Physics*, vol. 8, pp. 25–33, 2019.

[89] Z. Han, Z. Gui, Y. B. Zhu et al., "The electronic transport channel protection and tuning in real space to boost the thermoelectric performance of Mg$_{3+\delta}$Sb$_{2-y}$Bi$_y$ near room temperature," *Research*, vol. 2020, Article ID 1672051, 12 pages, 2020.

[90] L. R. Jørgensen, J. Zhang, C. B. Zeuthen, and B. B. Iversen, "Thermal stability of Mg$_3$Sb$_{1.475}$Bi$_{0.475}$Te$_{0.05}$ high perfor-

mance *n*-type thermoelectric investigated through powder X-ray diffraction and pair distribution function analysis," *Journal of Materials Chemistry A*, vol. 6, no. 35, pp. 17171–17176, 2018.

[91] L. Song, J. Zhang, and B. B. Iversen, "Thermal stability of *p*-type Ag-doped Mg3Sb2 thermoelectric materials investigated by powder X-ray diffraction," *Physical Chemistry Chemical Physics*, vol. 21, no. 8, pp. 4295–4305, 2019.

[92] X. Shi, C. Sun, X. Zhang et al., "Efficient Sc-doped Mg$_{3.05-x}$Sc$_x$SbBi thermoelectrics near room temperature," *Chemistry of Materials*, vol. 31, no. 21, pp. 8987–8994, 2019.

[93] F. Zhang, C. Chen, H. Yao et al., "High-performance N-type Mg$_3$Sb$_2$ towards thermoelectric application near room temperature," *Advanced Functional Materials*, vol. 30, no. 5, Article ID 1906143, 2019.

[94] W. Peng, G. Petretto, G.-M. Rignanese, G. Hautier, and A. Zevalkink, "An unlikely route to low lattice thermal conductivity: small atoms in a simple layered structure," *Joule*, vol. 2, no. 9, pp. 1879–1893, 2018.

[95] J. J. Kuo, S. D. Kang, K. Imasato et al., "Grain boundary dominated charge transport in Mg$_3$Sb$_2$-based compounds," *Energy & Environmental Science*, vol. 11, no. 2, pp. 429–434, 2018.

[96] K. Imasato, C. Fu, Y. Pan et al., "Metallic *n*-type Mg$_3$Sb$_2$ Single crystals demonstrate the absence of ionized impurity scattering and enhanced thermoelectric performance," *Advanced Materials*, vol. 32, no. 16, Article ID e1908218, 2020.

[97] S. Ohno, K. Imasato, S. Anand et al., "Phase boundary mapping to obtain *n*-type Mg$_3$Sb$_2$-based thermoelectrics," *Joule*, vol. 2, no. 1, pp. 141–154, 2018.

[98] J. J. Kuo, Y. Yu, S. D. Kang, O. Cojocaru-Mirédin, M. Wuttig, and G. J. Snyder, "Mg deficiency in grain boundaries of *n*-type Mg$_3$Sb$_2$ Identified by atom probe tomography," *Advanced Materials Interfaces*, vol. 6, no. 13, Article ID 1900429, 2019.

[99] J. Zhang, L. Song, and B. B. Iversen, "Insights into the design of thermoelectric Mg$_3$Sb$_2$ and its analogs by combining theory and experiment," *Npj Computational Materials*, vol. 5, no. 1, 2019.

[100] X. Shi, X. Wang, W. Li, and Y. Pei, "Advances in thermoelectric Mg3Sb2 and its derivatives," *Small Methods*, vol. 2, no. 10, Article ID 1800022, 2018.

[101] "The periodic table of the elements," June 2020, https://www.webelements.com/.

[102] "Shannon-Prewitt effective ionic radius navigation," September 2020, http://www.knowledgedoor.com/2/elements_handbook/shannon-prewitt_effective_ionic_radius.html.

[103] R. H. Perry, *Perry's Chemical Engineers' Handbook*, D. W. Green, Ed., McGraw-Hill, 7th edition, 1997.

[104] A. C. Barnes, C. Guo, and W. S. Howells, "Fast-ion conduction and the structure of beta -Mg$_3$Bi$_2$," *Journal of Physics: Condensed Matter*, vol. 6, no. 32, pp. L467–L471, 1994.

[105] W. S. Howells, A. C. Barnes, and M. Hamilton, "Quasielastic neutron scattering and the dynamics of Mg^{2+} in the fast ion and liquid phases of Mg$_3$Bi$_2$," *Physica B: Condensed Matter*, vol. 266, no. 1-2, pp. 97–99, 1999.

[106] J. Lee, B. Monserrat, I. D. Seymour, Z. Liu, S. E. Dutton, and C. P. Grey, "An ab initio investigation on the electronic structure, defect energetics, and magnesium kinetics in Mg$_3$Bi$_2$," *Journal of Materials Chemistry A*, vol. 6, no. 35, pp. 16983–16991, 2018.

[107] Z. Meng, D. Foix, N. Brun et al., "Alloys to replace Mg anodes in efficient and practical Mg-ion/sulfur batteries," *ACS Energy Letters*, vol. 4, no. 9, pp. 2040–2044, 2019.

[108] M. Martinez-Ripoll, A. Haase, and G. Brauer, "The crystal structure of α-Mg$_3$Sb$_2$," *Acta Crystallographica Section B Structural Crystallography and Crystal Chemistry*, vol. 30, no. 8, pp. 2006–2009, 1974.

[109] F. Predel, *Phase Equilibria, Crystallographic and Thermodynamic Data of Binary Alloys*, Springer-Verlag, Berlin Heidelberg, 2016.

[110] Y. Imai and A. Watanabe, "Electronic structures of Mg$_3$Pn$_2$ (Pn = N, P, As, Sb and Bi) and Ca$_3$N$_2$ calculated by a first-principle pseudopotential method," *Journal of Materials Science*, vol. 41, no. 8, pp. 2435–2441, 2006.

[111] L. G. Sevast'yanova, O. V. Kravchenko, O. K. Gulish, V. A. Stupnikov, M. E. Leonova, and M. G. Zhizhin, "Binary and ternary compounds in the Mg-Sb-B and Mg-Bi-B systems as catalysts for the synthesis of cubic BN," *Inorganic Materials*, vol. 42, no. 8, pp. 863–866, 2006.

[112] M. Sedighi, B. Arghavani Nia, H. Zarringhalam, and R. Moradian, "Density functional theory study of the structural and electronic properties of Mg$_3$Bi$_2$ in hexagonal and cubic phases," *The European Physical Journal Applied Physics*, vol. 61, no. 1, Article ID 10103, p. 10103, 2013.

[113] C. Zheng, R. Hoffmann, R. Nesper, and H. G. von Schnering, "Site preferences and bond length differences in CaAl$_2$Si$_2$-type Zintl compounds," *Journal of the American Chemical Society*, vol. 108, no. 8, pp. 1876–1884, 1986.

[114] J. Sun and D. J. Singh, "Thermoelectric properties of AMg$_2$X$_2$, AZn$_2$Sb$_2$ (A = Ca, Sr, Ba; X = Sb, Bi), and Ba$_2$ZnX$_2$ (X = Sb, Bi) Zintl compounds," *Journal of Materials Chemistry A*, vol. 5, no. 18, pp. 8499–8509, 2017.

[115] K. Imasato, M. Wood, J. J. Kuo, and G. J. Snyder, "Improved stability and high thermoelectric performance through cation site doping in n-type La-doped Mg$_3$Sb$_{1.5}$Bi$_{0.5}$," *Journal of Materials Chemistry A*, vol. 6, no. 41, pp. 19941–19946, 2018.

[116] X. Sun, X. Li, J. Yang et al., "Achieving band convergence by tuning the bonding ionicity in n-type Mg$_3$Sb$_2$," *Journal of Computational Chemistry*, vol. 40, no. 18, pp. 1693–1700, 2019.

[117] M. Wood, K. Imasato, S. Anand, J. Yang, and G. J. Snyder, "The importance of the Mg–Mg interaction in Mg$_3$Sb$_2$–Mg$_3$Bi$_2$ shown through cation site alloying," *Journal of Materials Chemistry A*, vol. 8, no. 4, pp. 2033–2038, 2020.

[118] F. Zhang, C. Chen, S. Li et al., "Enhanced thermoelectric performance in N-type Mg$_{3.2}$Sb$_{1.5}$Bi$_{0.5}$ by La or Ce doping into Mg," *Advanced Electronic Materials*, vol. 6, no. 3, Article ID 1901391, 2020.

[119] S.-Q. Xia, P. King, and S. Bobev, "Mg and Zn disorder in Mg$_{1.59(1)}$Zn$_{1.41(1)}$Sb$_2$," *Acta Crystallographica Section E: Structure Reports Online*, vol. 62, no. 9, pp. i184–i186, 2006.

[120] S.-Q. Xia, C. Myers, and S. Bobev, "Combined experimental and density functional theory studies on the crystal structures and magnetic properties of Mg(Mg$_{1-x}$Mn$_x$)$_2$Sb$_2$ (x $\approx$0.25) and BaMn$_2$Sb$_2$," *European Journal of Inorganic Chemistry*, vol. 2008, no. 27, pp. 4262–4269, 2008.

[121] J. Zhang, L. Song, M. Sist, K. Tolborg, and B. B. Iversen, "Chemical bonding origin of the unexpected isotropic physical properties in thermoelectric Mg$_3$Sb$_2$ and related materials," *Nature Communications*, vol. 9, no. 1, Article ID 4716, 2018.

[122] B. R. Ortiz, P. Gorai, T. Braden et al., "Discovery of n-type Zintl phases RbAlSb$_4$, RbGaSb$_4$, CsAlSb$_4$, and CsGaSb$_4$," *ACS Applied Energy Materials*, vol. 3, no. 3, pp. 2182–2191, 2020.

[123] C. Zheng and R. Hoffmann, "Complementary local and extended views of bonding in the ThCr$_2$Si$_2$ and CaAl$_2$Si$_2$ structures," *Journal of Solid State Chemistry*, vol. 72, no. 1, pp. 58–71, 1988.

[124] S. M. Kauzlarich, A. Zevalkink, E. Toberer, and G. J. Snyder, "Zintl phases: recent developments in thermoelectrics and future outlook," in *Thermoelectric Materials and Devices*, I. Nandhakumar, N. M. White, and S. Beeby, Eds., pp. 1–26, The Royal Society of Chemistry, 2017.

[125] K. Momma and F. Izumi, "VESTA 3for three-dimensional visualization of crystal, volumetric and morphology data," *Journal of Applied Crystallography*, vol. 44, no. 6, pp. 1272–1276, 2011.

[126] J. Li, S. Zhang, B. Wang et al., "Designing high-performance n-type Mg$_3$Sb$_2$-based thermoelectric materials through forming solid solutions and biaxial strain," *Journal of Materials Chemistry A*, vol. 6, no. 41, pp. 20454–20462, 2018.

[127] X. Tan, G.-Q. Liu, H. Hu, H. Shao, J. Xu, and J. Jiang, "Band engineering and crystal field screening in thermoelectric Mg$_3$Sb$_2$," *Journal of Materials Chemistry A*, vol. 7, no. 15, pp. 8922–8928, 2019.

[128] X. Zhang, L. Jin, X. Dai, and G. Liu, "Topological type-II nodal line semimetal and Dirac semimetal state in stable kagome compound Mg$_3$Bi$_2$," *The Journal of Physical Chemistry Letters*, vol. 8, no. 19, pp. 4814–4819, 2017.

[129] T.-R. Chang, I. Pletikosic, T. Kong et al., "Realization of a type-II nodal-line semimetal in Mg$_3$Bi$_2$," *Advanced Science*, vol. 6, no. 4, Article ID 1800897, 2019.

[130] T. Zhou, X.-G. Zhu, M. Tong et al., "Experimental evidence of topological surface states in Mg$_3$Bi$_2$ Films grown by molecular beam epitaxy," *Chinese Physics Letters*, vol. 36, no. 11, Article ID 117303, 2019.

[131] F. Ahmadpour, T. Kolodiazhnyi, and Y. Mozharivskyj, "Structural and physical properties of Mg$_{3-x}$Zn$_x$Sb$_2$ (x =0–1.34)," *Journal of Solid State Chemistry*, vol. 180, no. 9, pp. 2420–2428, 2007.

[132] D. M. Verbrugge and J. B. Van Zytveld, "Electronic properties of liquid MgSb," *Journal of Non-Crystalline Solids*, vol. 156-158, pp. 736–739, 1993.

[133] S. Huang, Z. Wang, R. Xiong, H. Yu, and J. Shi, "Significant enhancement in thermoelectric performance of Mg$_3$Sb$_2$ from bulk to two-dimensional mono layer," *Nano Energy*, vol. 62, pp. 212–219, 2019.

[134] F. Meng, S. Sun, J. Ma, C. Chronister, J. He, and W. Li, "Anisotropic thermoelectric figure-of-merit in Mg$_3$Sb$_2$," *Materials Today Physics*, vol. 13, Article ID 100217, 2020.

[135] J. Xin, G. Li, G. Auffermann et al., "Growth and transport properties of Mg$_3$X$_2$ (X = Sb, Bi) single crystals," *Materials Today Physics*, vol. 7, pp. 61–68, 2018.

[136] E. S. Toberer, A. Zevalkink, and G. J. Snyder, "Phonon engineering through crystal chemistry," *Journal of Materials Chemistry*, vol. 21, no. 40, pp. 15843–15852, 2011.

[137] T. M. Tritt, *Thermal Conductivity: Theory, Properties, and Applications*, Springer, 2004.

[138] D. T. Morelli, V. Jovovic, and J. P. Heremans, "Intrinsically minimal thermal conductivity in CubicI–V–VI2Semiconductors," *Physical Review Letters*, vol. 101, no. 3, Article ID 035901, 2008.

[139] M. Roufosse and P. G. Klemens, "Thermal conductivity of complex dielectric crystals," *Physical Review B*, vol. 7, no. 12, pp. 5379–5386, 1973.

[140] L.-D. Zhao, J. He, D. Berardan et al., "BiCuSeO oxyselenides: new promising thermoelectric materials," *Energy & Environmental Science*, vol. 7, no. 9, pp. 2900–2924, 2014.

[141] Y. Xiao, C. Chang, Y. Pei et al., "Origin of low thermal conductivity in SnSe," *Physical Review B*, vol. 94, no. 12, Article ID 125203, 2016.

[142] Y. Wang, X. Zhang, Y. Wang, H. Liu, and J. Zhang, "Enhanced thermoelectric properties of *n*-type Mg_3Sb_2 by excess magnesium and tellurium doping," *Physica Status Solidi (A)*, vol. 216, no. 6, Article ID 1800811, 2019.

[143] M. T. Agne, K. Imasato, S. Anand et al., "Heat capacity of Mg_3Sb_2, Mg_3Bi_2, and their alloys at high temperature," *Materials Today Physics*, vol. 6, pp. 83–88, 2018.

[144] O. Delaire, J. Ma, K. Marty et al., "Giant anharmonic phonon scattering in PbTe," *Nature Materials*, vol. 10, no. 8, pp. 614–619, 2011.

[145] J. Ma, O. Delaire, A. F. May et al., "Glass-like phonon scattering from a spontaneous nanostructure in $AgSbTe_2$," *Nature Nanotechnology*, vol. 8, no. 6, pp. 445–451, 2013.

[146] S. Song, J. Mao, J. Shuai et al., "Study on anisotropy of *n*-type Mg_3Sb_2-based thermoelectric materials," *Applied Physics Letters*, vol. 112, no. 9, Article ID 092103, 2018.

[147] L. Hu, T. Zhu, X. Liu, and X. Zhao, "Point defect engineering of high-performance bismuth-telluride-based thermoelectric materials," *Advanced Functional Materials*, vol. 24, no. 33, pp. 5211–5218, 2014.

[148] R. Deng, X. Su, Z. Zheng et al., "Thermal conductivity in $Bi_{0.5}Sb_{1.5}Te_{3+x}$ and the role of dense dislocation arrays at grain boundaries," *Science Advances*, vol. 4, no. 6, Article ID eaar5606, 2018.

[149] J. Yang, G. P. Meisner, and L. Chen, "Strain field fluctuation effects on lattice thermal conductivity of ZrNiSn-based thermoelectric compounds," *Applied Physics Letters*, vol. 85, no. 7, pp. 1140–1142, 2004.

[150] Y. Liu, H. Xie, C. Fu, G. J. Snyder, X. Zhao, and T. Zhu, "Demonstration of a phonon-glass electron-crystal strategy in (Hf,Zr)NiSn half-Heusler thermoelectric materials by alloying," *Journal of Materials Chemistry A*, vol. 3, no. 45, pp. 22716–22722, 2015.

[151] R. Gurunathan, R. Hanus, M. Dylla, A. Katre, and G. J. Snyder, "Analytical models of phonon-point-defect scattering," *Physical Review Applied*, vol. 13, no. 3, Article ID 034011, 2020.

[152] Q. Zhang, T. J. Zhu, A. J. Zhou, H. Yin, and X. B. Zhao, "Preparation and thermoelectric properties of $Mg_2Si_{1-x}Sn_x$," *Physica Scripta*, vol. T129, no. T129, pp. 123–126, 2007.

[153] S.-I. Yi, V. Attari, M. Jeong et al., "Strain-induced suppression of the miscibility gap in nanostructured Mg_2Si–Mg_2Sn solid solutions," *Journal of Materials Chemistry A*, vol. 6, no. 36, pp. 17559–17570, 2018.

[154] M. Yasseri, A. Sankhla, H. Kamila et al., "Solid solution formation in Mg_2(Si,Sn) and shape of the miscibility gap," *Acta Materialia*, vol. 185, pp. 80–88, 2020.

[155] M. Schwall and B. Balke, "Phase separation as a key to a thermoelectric high efficiency," *Physical Chemistry Chemical Physics*, vol. 15, no. 6, pp. 1868–1872, 2013.

[156] A. Page, A. Van der Ven, P. F. P. Poudeu, and C. Uher, "Origins of phase separation in thermoelectric (Ti, Zr, Hf)NiSn half-Heusler alloys from first principles," *Journal of Materials Chemistry A*, vol. 4, no. 36, pp. 13949–13956, 2016.

[157] E. Rausch, B. Balke, J. M. Stahlhofen, S. Ouardi, U. Burkhardt, and C. Felser, "Fine tuning of thermoelectric performance in phase-separated half-Heusler compounds," *Journal of Materials Chemistry C*, vol. 3, no. 40, pp. 10409–10414, 2015.

[158] J. M. Mena, E. Rausch, S. Ouardi et al., "Miscibility gap in the phase diagrams of thermoelectric half-Heusler materials $CoTi_{1-x}Y_xSb$ (Y = Sc, V, Mn, Fe)," *Journal of Electronic Materials*, vol. 45, no. 3, pp. 1382–1388, 2016.

[159] Y. Liu, C. Fu, K. Xia et al., "Lanthanide contraction as a design factor for high-performance half-Heusler thermoelectric materials," *Advanced Materials*, vol. 30, no. 32, Article ID 1800881, 2018.

[160] H. Wang, A. D. LaLonde, Y. Pei, and G. J. Snyder, "The criteria for beneficial disorder in thermoelectric solid solutions," *Advanced Functional Materials*, vol. 23, no. 12, pp. 1586–1596, 2013.

[161] R. Hanus, M. T. Agne, A. J. E. Rettie et al., "Lattice softening Significantly reduces thermal conductivity and leads to high thermoelectric Efficiency," *Advanced Materials*, vol. 31, no. 21, Article ID 1900108, 2019.

[162] J. Zhang, L. Song, G. K. H. Madsen et al., "Designing high-performance layered thermoelectric materials through orbital engineering," *Nature Communications*, vol. 7, no. 1, Article ID 10892, 2016.

[163] J. Li, S. Zheng, T. Fang, L. Yue, S. Zhang, and G. Lu, "Computational prediction of a highZTof *n*-type Mg_3Sb_2-based compounds with isotropic thermoelectric conduction performance," *Physical Chemistry Chemical Physics*, vol. 20, no. 11, pp. 7686–7693, 2018.

[164] A. F. May and G. J. Snyder, "Introduction to modeling thermoelectric transport at high temperatures," in *Materials, Preparation, and Characterization in Thermoelectrics*, D. M. Rowe, Ed., pp. 1–18, Taylor & Francis Group, 2017.

[165] A. F. May, E. S. Toberer, A. Saramat, and G. J. Snyder, "Characterization and analysis of thermoelectric transport inntypeBa$_8$Ga$_{16-x}$Ge$_{30+x}$," *Physical Review B*, vol. 80, no. 12, Article ID 125205, 2009.

[166] K. Imasato, S. D. Kang, S. Ohno, and G. J. Snyder, "Band engineering in Mg_3Sb_2 by alloying with Mg3Bi2for enhanced thermoelectric performance," *Materials Horizons*, vol. 5, no. 1, pp. 59–64, 2018.

[167] G. J. Snyder, A. H. Snyder, M. Wood, R. Gurunathan, B. H. Snyder, and C. Niu, "Weighted mobility," *Advanced Materials*, vol. 32, no. 25, Article ID 2001537, 2020.

[168] C. Fu, T. Zhu, Y. Liu, H. Xie, and X. Zhao, "Band engineering of high performance p-type FeNbSb based half-Heusler thermoelectric materials for figure of merit zT > 1," *Energy & Environmental Science*, vol. 8, no. 1, pp. 216–220, 2015.

[169] J. O. Sofo and G. D. Mahan, "Optimum band gap of a thermoelectric material," *Physical Review B*, vol. 49, no. 7, pp. 4565–4570, 1994.

[170] Y. Pei, Z. M. Gibbs, A. Gloskovskii, B. Balke, W. G. Zeier, and G. J. Snyder, "Optimum carrier concentration in *n*-type PbTe thermoelectrics," *Advanced Energy Materials*, vol. 4, no. 13, Article ID 1400486, 2014.

[171] P. Gorai, E. S. Toberer, and V. Stevanović, "Effective *n*-type doping of Mg_3Sb_2 with group-3 elements," *Journal of Applied Physics*, vol. 125, no. 2, Article ID 025105, 2019.

[172] "Periodic table of atomic orbital energies," June 2020, http://www.graylark.com/eve/orbital-energies-table.html.

[173] Y. Wang, X. Zhang, Y. Liu, Y. Wang, H. Liu, and J. Zhang, "Enhanced electrical transport performance through cation site doping in Y-doped $Mg_{3.2}Sb_2$," *Journal of Materiomics*, vol. 6, no. 1, pp. 216–223, 2020.

[174] K. W. Böer and U. W. Pohl, *Semiconductor Physics*, Springer, 2018.

[175] Q. Ren, C. Fu, Q. Qiu et al., "Establishing the carrier scattering phase diagram for ZrNiSn-based half-Heusler thermoelectric materials," *Nature Communication*, vol. 11, no. 1, Article ID 3142, 2020.

[176] H. Wang, Y. Pei, A. D. LaLonde, and G. J. Snyder, "Material design considerations based on thermoelectric quality factor," in *Thermoelectric Nanomaterials: Materials Design and Applications*, K. K. TMs, Ed., pp. 3–32, Springer, 2013.

[177] X. Shi, C. Sun, Z. Bu et al., "Revelation of inherently high mobility enables Mg_3Sb_2 as a sustainable alternative to n-Bi_2Te_3Thermoelectrics," *Advanced Science*, vol. 6, no. 16, article 1802286, 2019.

[178] J. Shuai, B. Ge, J. Mao, S. Song, Y. Wang, and Z. Ren, "Significant role of Mg stoichiometry in designing high thermoelectric performance for $Mg_3(Sb,Bi)_2$-based *n*-type Zintls," *Journal of American Chemical Society*, vol. 140, no. 5, pp. 1910–1915, 2018.

[179] J. J. Kuo, M. Wood, T. J. Slade, M. G. Kanatzidis, and G. J. Snyder, "Systematic over-estimation of lattice thermal conductivity in materials with electrically-resistive grain boundaries," *Energy & Environmental Science*, vol. 13, no. 4, pp. 1250–1258, 2020.

[180] T. Watanabe, "Grain boundary engineering: historical perspective and future prospects," *Journal of Materials Science*, vol. 46, no. 12, pp. 4095–4115, 2011.

[181] P. R. Cantwell, M. Tang, S. J. Dillon, J. Luo, G. S. Rohrer, and M. P. Harmer, "Grain boundary complexions," *Acta Materialia*, vol. 62, pp. 1–48, 2014.

[182] X. Su, P. Wei, H. Li et al., "Multi-scale microstructural thermoelectric materials: transport behavior, non-equilibrium preparation, and applications," *Advanced Materials*, vol. 29, no. 20, Article ID 1602013, 2017.

[183] Z. Chen, Z. Jian, W. Li et al., "Lattice dislocations enhancing thermoelectric PbTe in addition to band convergence," *Advanced Materials*, vol. 29, no. 23, Article ID 1606768, 2017.

[184] Y. Yu, C. Zhou, S. Zhang et al., "Revealing nano-chemistry at lattice defects in thermoelectric materials using atom probe tomography," *Materials Today*, vol. 32, pp. 260–274, 2020.

[185] H. Wu, Y. Zhang, S. Ning, L. D. Zhao, and S. J. Pennycook, "Seeing atomic-scale structural origins and foreseeing new pathways to improved thermoelectric materials," *Materials Horizons*, vol. 6, no. 8, pp. 1548–1570, 2019.

[186] C. Zhao, Z. Li, T. Fan, C. Xiao, and Y. Xie, "Defects engineering with multiple dimensions in thermoelectric materials," *Research*, vol. 2020, article 9652749, 23 pages, 2020.

[187] J. Horák, K. Čermák, and L. Koudelka, "Energy formation of antisite defects in doped Sb_2Te_3 and Bi_2Te_3 crystals," *Journal of Physics and Chemistry of Solids*, vol. 47, no. 8, pp. 805–809, 1986.

[188] S. Cho, Y. Kim, A. DiVenere, G. K. Wong, J. B. Ketterson, and J. R. Meyer, "Antisite defects of Bi_2Te_3 thin films," *Applied Physics Letters*, vol. 75, no. 10, pp. 1401–1403, 1999.

[189] H. Xie, H. Wang, C. Fu et al., "The intrinsic disorder related alloy scattering in ZrNiSn half-Heusler thermoelectric materials," *Scientific Reports*, vol. 4, no. 1, Article ID 6888, 2015.

[190] W. G. Zeier, J. Schmitt, G. Hautier et al., "Engineering half-Heusler thermoelectric materials using Zintl chemistry," *Nature Reviews Materials*, vol. 1, no. 6, Article ID 16032, 2016.

[191] Z. Liu, H. Geng, J. Mao et al., "Understanding and manipulating the intrinsic point defect in α-MgAgSb for higher thermoelectric performance," *Journal of Materials Chemistry A*, vol. 4, no. 43, pp. 16834–16840, 2016.

[192] J. Zhang, L. Song, and B. B. Iversen, "Rapid one-step synthesis and compaction of high-performance *n*-type Mg_3Sb_2 Thermoelectrics," *Angewandte Chemie International Edition in English*, vol. 59, no. 11, pp. 4278–4282, 2020.

[193] J. Li, F. Jia, S. Zhang et al., "The manipulation of substitutional defects for realizing high thermoelectric performance in Mg_3Sb_2-based Zintl compounds," *Journal of Materials Chemistry A*, vol. 7, no. 33, pp. 19316–19323, 2019.

[194] J. Mao, Y. Wu, S. Song et al., "Defect engineering for realizing high thermoelectric performance in *n*-type Mg_3Sb_2-based materials," *ACS Energy Letters*, vol. 2, no. 10, pp. 2245–2250, 2017.

[195] P. Gorai, B. R. Ortiz, E. S. Toberer, and V. Stevanović, "Investigation of *n*-type doping strategies for Mg_3Sb_2," *Journal of Materials Chemistry A*, vol. 6, no. 28, pp. 13806–13815, 2018.

[196] J. Li, S. Zhang, S. Zheng et al., "Defect chemistry for N-type doping of Mg_3Sb_2-based thermoelectric materials," *The Journal of Physical Chemistry C*, vol. 123, no. 34, pp. 20781–20788, 2019.

[197] H. Wang, X. Cao, Y. Takagiwa, and G. J. Snyder, "Higher mobility in bulk semiconductors by separating the dopants from the charge-conducting band – a case study of thermoelectric PbSe," *Materials Horizons*, vol. 2, no. 3, pp. 323–329, 2015.

[198] Q. H. Zhang, X. Y. Huang, S. Q. Bai, X. Shi, C. Uher, and L. D. Chen, "Thermoelectric devices for power generation: recent progress and future challenges," *Advanced Engineering Materials*, vol. 18, no. 2, pp. 194–213, 2016.

[199] W. Liu, Q. Jie, H. S. Kim, and Z. Ren, "Current progress and future challenges in thermoelectric power generation: from materials to devices," *Acta Materialia*, vol. 87, pp. 357–376, 2015.

[200] R. He, G. Schierning, and K. Nielsch, "Thermoelectric devices: a review of devices, architectures, and contact optimization," *Advanced Materials Technologies*, vol. 3, no. 4, Article ID 1700256, 2018.